

To Appear in the *Astrophysical Journal*

# A Study of the Reionization History of Intergalactic Helium with *FUSE* and *VLT*<sup>1</sup>

W. Zheng<sup>2</sup>, G. A. Kriss<sup>2,3</sup>, J.-M. Deharveng<sup>4</sup>, W. V. Dixon<sup>2</sup>, J. W. Kruk<sup>2</sup>, J. M. Shull<sup>5,6</sup>,  
M. L. Giroux<sup>7</sup>, D. C. Morton<sup>8</sup>, G. M. Williger<sup>2</sup>, S. D. Friedman<sup>3</sup>, and H. W. Moos<sup>2</sup>

## ABSTRACT

We obtained high-resolution *FUSE* ( $R \sim 20,000$ ) and *VLT* ( $R \sim 45,000$ ) spectra of the quasar HE2347–4342 to study the properties of the intergalactic medium between redshifts  $z = 2.0 - 2.9$ . The high-quality optical spectrum allows us to identify approximately 850 H I absorption lines with column densities between  $N \sim 5 \times 10^{11}$  and  $10^{18} \text{ cm}^{-2}$ . The reprocessed *FUSE* spectrum extends the wavelength coverage of the He II absorption down to an observed wavelength

---

<sup>1</sup>Based on observations made for the Guaranteed Time Team by the NASA-CNES-CSA *FUSE* mission, operated by the Johns Hopkins University under NASA contract NAS5-32985; Ultraviolet-Visual Echelle Spectrograph observations performed at the European Southern Observatory, Paranal, Chile, within the program 68.A-0230; and observations with the NASA/ESA *Hubble Space Telescope*, obtained at the Space Telescope Science Institute, which is operated by the Association of Universities of Research in Astronomy, Inc., under NASA contract NAS5-26555.

<sup>2</sup>Center for Astrophysical Sciences, Department of Physics and Astronomy, The Johns Hopkins University, Baltimore, MD 21218 (zheng@pha.jhu.edu; wvd@pha.jhu.edu; kruk@pha.jhu.edu; williger@pha.jhu.edu; hwm@pha.jhu.edu)

<sup>3</sup>Space Telescope Science Institute, 3700 San Martin Drive, Baltimore, MD 21218 (gak@stsci.edu; friedman@stsci.edu)

<sup>4</sup>Laboratoire d'Astrophysique de Marseille, BP 8, 13376 Marseille Cedex 12, France (jean-michel.deharveng@oamp.fr)

<sup>5</sup>CASA, Department of Astrophysical and Planetary Sciences, University of Colorado, Boulder, CO 80309 (mshull@casa.colorado.edu)

<sup>6</sup>Also at JILA, University of Colorado and National Institute of Standards and Technology

<sup>7</sup>Department of Physics and Astronomy, Box 70652, East Tennessee State University, Johnson City, TN 37614 (giroux@polar.etsu.edu)

<sup>8</sup>Herzberg Institute of Astrophysics, National Research Council, Victoria, BC V9E 2E7, Canada (don.morton@nrc.gc.ca)

of 920 Å. Source flux is detected to restframe wavelengths as short as  $\sim 237$  Å. Approximately 1400 He II absorption lines are identified, including 917 He II Ly $\alpha$  systems and some of their He II Ly $\beta$ , Ly $\gamma$ , and Ly $\delta$  counterparts. The ionization structure of He II is complex, with approximately 90 absorption lines that are not detected in the hydrogen spectrum. These features may represent the effect of soft ionizing sources. The ratio  $\eta = N(\text{He II})/N(\text{H I})$  varies approximately from unity to more than a thousand, with a median value of 62 and a distribution consistent with the intrinsic spectral indices of quasars. This provides evidence that the dominant ionizing field is from the accumulated quasar radiation, with contributions from other soft sources such as star-forming regions and obscured AGN, which do not ionize helium. We find an evolution in  $\eta$  toward smaller values at lower redshift, with the gradual disappearance of soft components. At redshifts  $z > 2.7$ , the large but finite increase in the He II opacity,  $\tau = 5 \pm 1$ , suggests that we are viewing the end stages of a reionization process that began at an earlier epoch. Fits of the absorption profiles of unblended lines indicate comparable velocities between hydrogen and He<sup>+</sup> ions. For line widths  $b_{\text{He}^+} = \xi b_{\text{H}}$ , we find  $\xi = 0.95 \pm 0.12$ , indicating a velocity field in the intergalactic medium dominated by turbulence. At hydrogen column densities  $N < 3 \times 10^{12} \text{ cm}^{-2}$  the number of forest lines shows a significant deficit relative to a power law, and becomes negligible below  $N = 10^{11} \text{ cm}^{-2}$ .

*Subject headings:* dark matter — intergalactic medium — quasars: absorption lines — quasars: individual (HE2347–4342) — ultraviolet: general

## 1. INTRODUCTION

According to current models of cold-dark-matter structure formation, the first generation of massive baryonic objects, i.e., stars, galaxies and quasars, was formed in the early universe as the result of density fluctuations of the intergalactic medium (IGM; Zhang et al. 1995; Miralda-Escudé et al. 1996; Bi and Davidsen 1997). The radiation from these objects gradually ionized the surrounding IGM, ending the so-called “dark age.” Most models predict that the intergalactic hydrogen was ionized at  $z \sim 7 - 10$ , and helium at  $z \sim 3 - 4$  (Loeb and Barkana 2001; Wyithe and Loeb 2003, and references therein). The recent *WMAP* results (Spergel et al. 2003) provide evidence that the IGM reionization may have started at  $z \sim 17$ . Cen (2003) suggests that there may have been a second stage of hydrogen reionization that took place at  $z \sim 6$ , and Venkatesan et al. (2003) suggest that helium may also have been reionized twice, partially by an early generation of Population III stars, and

subsequently by quasar radiation at  $z < 5$ .

Our knowledge of the IGM has been derived largely from the Ly $\alpha$  forest absorption of neutral hydrogen. The expansion of the universe following reionization leads to a rapid drop in the hydrogen Ly $\alpha$  effective optical depth of the IGM,  $\tau \propto (1+z)^{3.5}$  (Press et al. 1993). The number density of forest lines also increases toward lower column density, with  $dn/dN \propto N^{-1.5}$  (Kim et al. 2002). Lines at a column density of  $N \sim 10^{13} \text{ cm}^{-2}$  represent the mean density the IGM. The underdense regions, represented by hydrogen column densities below  $N \sim 10^{12} \text{ cm}^{-2}$ , have been largely undetected. Throughout this paper, the column density  $N$  refers to hydrogen, unless noted otherwise.

The IGM can also be traced by He II absorption, which is far more sensitive than H I. Under the hard photoionizing conditions at  $z \sim 3$ , He $^+$  outnumbers H $^0$  by a factor  $\eta$  of the order of 100 (Davidsen et al. 1996; Kriss et al. 2001). The He II optical depth is therefore  $\eta/4$  or approximately 25 times greater than that of H I for turbulent line broadening and  $\eta/2$  for thermal broadening. For a tenuous structure that produces an H I optical depth less than 0.01, even the best optical spectra may not provide a significant detection. But the corresponding He II optical depth, at 0.25, can be detected at a moderate signal-to-noise (S/N) ratio. He II absorption is therefore an effective tracer of the low-density structures that fill  $\sim 70\%$  of the volume of the universe at  $z \sim 3$ . Significant He II absorption exists even in the spectral voids where there are no detected Ly $\alpha$  forest lines. As Croft et al. (1997) show, each of several different CDM models can explain the distribution of the H I forest lines, but the various models predict different results for He II absorption.

The search for the He II Gunn-Peterson effect has yielded significant results in recent years. Jakobsen et al. (1994) reported a sharp flux cutoff at the He II Ly $\alpha$  wavelength  $304(1+z) \text{ \AA}$  in the spectrum of quasar Q0302-003 ( $z = 3.286$ ), obtained with *HST*. Follow-up observations at a higher S/N level and spectral resolution (Hogan et al. 1997; Heap et al. 2000) found an average He II optical depth  $\tau = 4.0 \pm 0.5$  at  $z \sim 3$ . At far-UV wavelengths below  $1200 \text{ \AA}$ , He II spectra exhibit a significantly lower He II opacity, enabling detailed studies of the ionization structure of the IGM. Hopkins Ultraviolet Telescope (HUT) observations of the luminous quasar HS1700+64 ( $z = 2.73$ , Davidsen et al. 1996) revealed an average He II optical depth of  $1.00 \pm 0.07$ , which suggests that the dominant ionization source at  $z \sim 2.5$  is from quasars instead of stars, but the low resolution of HUT does not allow a study of the individual absorption components.

The bright quasar HE2347-4342 ( $z = 2.885$ ,  $V = 16.1$ ; Reimers et al. 1997) is an extremely rare object that exhibits a clear line of sight at restframe wavelengths around  $300 \text{ \AA}$ . Its UV flux, at a level of  $2 \times 10^{-15} \text{ ergs s}^{-1} \text{ cm}^{-2} \text{ \AA}^{-1}$ , is the highest among the five quasars with known He II Ly $\alpha$  features (Jakobsen et al. 1994; Davidsen et al. 1996;

Reimers et al. 1997; Anderson et al. 1999; Zheng et al. 2004), enabling a high-resolution study of He II absorption with *FUSE*. Below a redshift of 2.7, Kriss et al. (2001) resolved the He II Ly $\alpha$  absorption as a discrete forest of absorption lines. The column-density ratio  $\eta = N(\text{He II})/N(\text{H I})$  ranges from  $\sim 1$  to  $> 1000$ , suggesting a mix of ionizing sources of radiation consisting of quasars and star-forming galaxies. However, approximately 50% of these lines do not have detectable H I counterparts in the *Keck* spectrum of this quasar. At higher redshifts, the He II absorption has a patchy structure, including regions with low He II opacity (“voids”) and regions with high opacity and no detectable flux (blacked-out “troughs”). Using high S/N *HST*/STIS observations of this region, Smette et al. (2002) found that the  $\eta$  value is generally high, but shows large variations, from  $\sim 30$  in the opacity gaps to a lower limit of 2300 at  $z \sim 2.86$  in a region that shows an extremely low H I opacity over a 6.5 Å spectral range. In order to explain the shape of the opacity gaps (absence of large individual absorption lines) at this and other wavelengths, they suggested that six bright soft ionization sources lie near the line of sight, for which the ratio between the numbers of H I- to He II-ionizing photons reaching the IGM is large.

This change in character of the He II absorption is similar to the large increases in Lyman series H I opacity at  $z > 6$  seen in several quasars discovered by the Sloan Digital Sky Survey (Becker et al. 2000; Fan et al. 2002; White et al. 2003). As these authors have suggested that reionization of the H I in the IGM occurred just prior to this epoch, it is likely that reionization of He<sup>+</sup> occurred slightly above a redshift of 3. Theoretical models (Haardt and Madau 1996; Fardal et al. 1998; Madau et al. 1999; Loeb and Barkana 2001; Wyithe and Loeb 2003) also indicate that the reionization of intergalactic helium took place later than hydrogen as the number of He II-ionizing photons is significantly smaller than that for hydrogen. These initial regions of He II ionization, however, would have recombined, and only reached full ionization at lower redshift during the quasar era. Indirect evidence based on an increase in H I line widths (Ricotti et al. 2000; Theuns et al. 2002) and a decrease in H I opacity (Bernardi et al. 2003) support the assumption that the final stage of He II reionization may have taken place at  $z \sim 3.2 - 3.4$ .

In this paper, we present results based on a reprocessed *FUSE* spectrum of HE2347–4342 and a new *VLT*/UVES echelle spectrum. Our previous paper (Kriss et al. 2001) used only the *FUSE* data from the LiF channels, and a modest S/N *Keck* echelle spectrum between 3800 and 6000 Å. The improved *FUSE* pipeline allows us to extract spectra from the SiC channels, which extend the wavelength coverage to the 912–1000 Å region. The expanded wavelength coverage enables us to study the evolution of intergalactic helium with redshift down to  $z = 2$ , and also to observe the Ly $\beta$  portion of the He II forest. Our new *VLT* spectrum spans the full redshift range covered by the *FUSE* data, and its higher S/N makes it possible to identify weak H I lines with He II counterparts that are not detectable in

the *Keck* spectrum. We follow the traditional approach in this paper of fitting individual spectral features in the *FUSE* and *VLT* spectra. In a separate paper, Shull et al. (2003) describe an independent analysis of the *FUSE* spectrum at redshift 2.3-2.9 and another set of *VLT*/UVES data using a non-parametric approach to study the opacity variations in the IGM. They also identify fluctuations in the ionizing radiation field on a fine-grained scale,  $\Delta z \sim 0.001$ .

Our discussion in this paper is organized as follows. In §2 we describe our reprocessing of the *FUSE* data, and our new *VLT*/UVES observations. In §3 we explain how we identify and fit individual spectral features in the *FUSE* and *VLT* spectra. In §4 we discuss the scientific results of our analysis, concentrating on the column-density distribution of Ly $\alpha$  absorbers (§4.1), the velocity field in the IGM (§4.2), the evolution of the ionization state of the IGM (§4.3), the evolution of the He II opacity (§4.4), and the approach to the He II reionization epoch (§4.5). Section 5 summarizes our results.

## 2. DATA

### 2.1. Ultraviolet Data

The *Far-Ultraviolet Spectroscopic Explorer* (*FUSE*) is a NASA-CNES-CSA mission dedicated to high-resolution spectroscopy between 905 and 1187 Å. It consists of two UV detectors, four Rowland-circle gratings and four mirrors. The LiF-coated optics yield a wavelength coverage of  $\sim 979 - 1187$  Å, and the SiC-coated optics cover  $\sim 905 - 1104$  Å. For a full description of *FUSE*, its mission, and its in-flight performance, see Moos et al. (2000) and Sahnou et al. (2000).

The *FUSE* observations of HE2347–4342 were carried out in three periods in 2000: June 27, August 18-25, and October 15-20. A total of 243 raw images were obtained, representing an exposure time of 619 kseconds, of which 431 kseconds were at night. While the *FUSE* detector background is intrinsically low, the source count level from HE2347–4342 is still weaker than the background because of the high spectral resolution. The key step in our data analysis is the background subtraction. The *FUSE* background consists of two components: the detector dark count and the scattered light. The dark count is roughly constant across the detector but varies in intensity with time. The scattered light during day time is an order of magnitude stronger than at night, and it produces considerable and different spatial structures across the detectors. The inclusion of the day portion would completely obscure the weak source structure. We therefore use only the night portion of the data.

Based on the data of this quasar from the LiF channels of *FUSE* and a *Keck* optical

spectrum, (Kriss et al. 2001) have reported a rich absorption structure that reflects a broad range of ionization level. The average value of  $\eta \sim 80$  is consistent with photoionization of the absorbing gas by a hard ionizing spectrum resulting from the integrated light of quasars. The presence of He II absorbers with no H I counterparts indicates that structure is present even in low-density regions.

A new version of the *FUSE* calibration software (CalFUSE v2.2) enables us to reprocess the data and improve its quality. We first process each of the 243 raw exposures, rejecting undesirable events such as detector count bursts. The processed spectra are then merged to form a final image with the highest S/N possible. From this image, we are able to model and subtract the background more accurately than before.

We perform the background subtraction using two parallel approaches, including the standard pipeline procedure and manual extraction. To extract the spectrum manually, we define respective background windows on both sides of the source extraction windows on the detector. The background variations are assumed to be linear across the spatial dimension (Y), and its slope is estimated from the two background windows. The background level at the extraction window is then interpolated at every wavelength unit along the dispersion direction (X). This method cannot be fully implemented for extraction windows near the detector edge. In such cases, we define two background windows on one side of the extraction window, calculate the slope of variations and extrapolate the background level at the source position. A pair of background windows is necessary because the background varies across the detector, even at a low level.

The manual extraction yields better results, as judged by the level of residual flux in the opaque portions of the He II absorption spectrum. The standard pipeline extraction, on the other hand, produces a better photometric agreement at long wavelengths in the region of overlap with the HST/STIS data. The final data we present here are based on the manual extraction using photometric corrections as described below.

For a given window position, we extract the data using different sets of detector pulse-height parameters (*FUSE* Observer’s Guide 2003): 4-16, 5-16, 7-15, and 8-12. In principle, dark current and photon events exhibit different pulse characteristics. By choosing a narrow band of the pulse height, one would be able to reduce the contribution of dark-current events. However, a fraction of the source counts would also be lost, leading to photometric inaccuracy. The standard parameters for the pulse height, between 4 and 16 counts, yield a flux level that is close to photometric. A pulse height range of 5–16, however, maximizes the S/N, so we choose this range and normalize the extracted spectrum to the same flux level as obtained using the photometric pulse height range of 4–16.

The full set of *FUSE* data consists of eight segments labeled LiF 1A, 1B, 2A, 2B and SiC 1A, 1B, 2A, 2B. Sky emission lines are removed from the spectra (Feldman et al. 2000). Significant airglow lines include He I  $\lambda 584$  (second order at  $1168 \text{ \AA}$ ), N I  $\lambda 1134$ , O I  $\lambda 989$  and the Lyman-series lines. The spectra are then binned to  $0.025 \text{ \AA}$ , and combined with their S/N as the weighting factor at every pixel. This level of binning gives critical sampling of two bins per  $R = 20,000$  resolution element provided by *FUSE*, and corresponds identically in velocity ( $\sim 7.5 \text{ km s}^{-1}$ ) to the  $0.1 \text{ \AA}$  bins we use in sampling the H I spectrum described later in §2.2. A typical S/N level per resolution element is 10 at the long wavelength part ( $\lambda > 1050 \text{ \AA}$ ), and 3 at the short wavelengths.

The spectral normalization involves two steps: First, we correct the zero level. While the spectra extracted with CalFUSE v2.2 improve upon earlier pipeline results, and our manual extraction technique is even better, there are still regions where the zero level is not perfect. This is particularly obvious in the SiC spectra from detector 1, where the SiC 1A and 1B extraction windows lie near the edge of the detector. We correct the zero level using the H I Ly $\alpha$  forest spectrum where there are many features with fully saturated absorption at the line center. It is reasonable to assume that their He II counterparts will also be completely absorbed at the line center, as the He II optical depth is considerably higher than that of the H I feature. We assume that these data points should have zero flux, and fit a smoothly varying polynomial to these low points to determine the zero-level correction. This correction is up to 10% of the maximum flux in the LiF data segments, and up to 40% in the SiC channels.

Secondly, we normalize the *FUSE* spectrum, assuming the intrinsic, unabsorbed spectrum is a reddened power law. Since more than a thousand He II absorption lines nearly blanket the entire *FUSE* spectrum, it is difficult to determine the continuum level from the *FUSE* spectrum itself. As described by Kriss et al. (2001), a pair of *HST*/STIS spectra are used to derive the intrinsic continuum. These data were obtained contemporaneously with the respective *FUSE* data and serve as a photometric standard for our extracted *FUSE* spectrum. A comparison between the STIS and *FUSE* spectra indicates that the photometric quality of the *FUSE* data is reasonably good, agreeing with the STIS data to within about 5% between  $1150$  and  $1187 \text{ \AA}$ . The best-fit power law is  $f_\lambda = 3.3 \times 10^{-15} (\lambda/1000 \text{ \AA})^{-2.4} \text{ ergs s}^{-1} \text{ cm}^{-2} \text{ \AA}^{-1}$ , with  $E(B-V)=0.014$ . An extrapolation of this continuum model serves as the baseline for the renormalization of our *FUSE* spectrum.

## 2.2. Optical Data

Optical echelle spectra of HE2347–4342 were obtained at the ESO *VLT*/UVES on 2001 November 23–24. The exposure time for each readout was 30 minutes, and the total exposure time was 8 hours. The sky was photometric. With a slit opening of 1 arcsecond, the spectral resolution is approximately 45,000. We used the blue instrument arm, consisting of a  $2048 \times 4096$  CCD detector, an echelle grating of  $41.59 \text{ line mm}^{-1}$ , and a cross disperser of  $600 \text{ line mm}^{-1}$  and blaze wavelength of  $4600 \text{ \AA}$ . With a central wavelength  $4200 \text{ \AA}$  for the cross disperser, the spectrum covers the wavelength range between  $3600$  and  $4800 \text{ \AA}$  in 31 orders, which corresponds to the entire He II  $\text{Ly}\alpha$  wavelength range studied with *FUSE* from  $z = 2.0$  to  $2.9$ . There are significant overlaps in wavelength coverage between adjacent orders. The wavelength calibration spectra were taken with the ThAr lamp.

Using IRAF tasks designed for echelle data, we processed the spectra. For each extraction segment, we used 10–15 pixels on both sides of the trace to derive the background. The final wavelength calibration is accurate to  $\sim 0.007 \text{ \AA}$ , and it has been corrected to vacuum wavelengths in a heliocentric reference frame. We normalized each individual echelle order with a polynomial, then rebinned them to  $0.1 \text{ \AA}$ . We then merged all 31 segments of normalized spectra, weighted by the individual S/N ratios. The S/N ratio in the merged spectrum is about 110 per  $0.1 \text{ \AA}$  bin at  $4700 \text{ \AA}$ , and about 46 at  $3850 \text{ \AA}$ . This is approximately 2.5 and 10 times that of the *Keck* data, respectively. Only the *VLT* data cover the wavelength range between  $3600$  and  $3800 \text{ \AA}$ . To improve the continuum fitting, this count spectrum is further normalized with a high-order polynomial across the entire wavelength range. Figure 1 displays the normalized *FUSE* and *VLT* spectra of HE2347–4342 across the full wavelength range covered by our new data.

## 3. LINE FITTING

We analyze the spectral features in the *FUSE* and *VLT* spectra using the IRAF task *Specfit* (Kriss 1994). Absorption features are fit with Gaussian profiles rather than Voigt profiles. This is a good approximation for line components with column densities below  $10^{15} \text{ cm}^{-2}$ . Saturated lines may be better represented by Voigt profiles, but it is not important for our purpose since our main goal is to study the weak absorption lines. Because of the large number of components and variables, we carry out the fitting procedure in 48 wavelength segments of approximately  $25 \text{ \AA}$  each.

Below  $3984 \text{ \AA}$  in the optical spectrum,  $\text{Ly}\beta$  absorption starts to appear. Line fitting in this region is carried out using both  $\text{Ly}\alpha$  and  $\text{Ly}\beta$  for each identified feature. Paired



absorption lines are fit using the same velocity width and column density, and their central wavelengths are tied to the ratio of their intrinsic wavelengths.

Free parameters in the fit are line width, column density, and the centroid wavelength. The weakest features that we are able to identify in the *VLT* spectrum have a column density  $N = 5 \times 10^{11} \text{ cm}^{-2}$ , mostly at wavelengths longward of 4400 Å. At the short-wavelength end, the minimum detectable column density is  $\sim 1.5 \times 10^{12} \text{ cm}^{-2}$ . The number of these weak lines and their fitted parameters are affected by the continuum level. The errors in their column densities may be as large as a factor of two. We identify metal lines as those with  $b$  values less than  $10 \text{ km s}^{-1}$ . A total of 852 Ly $\alpha$  absorption lines are present in the *VLT* spectrum over the full 3600-4750 Å wavelength range.

The initial line fits to the *FUSE* spectrum are based on our results from fitting the H I Ly $\alpha$  forest. For every H I absorption line, we define a He II counterpart with the same velocity width (see §4.2) and redshift, with only the column density allowed to vary. As described in Kriss et al. (2001), additional He II absorption lines are added in regions where the He II optical depth is so high that no known H I component can provide with reasonable  $\eta$  values. Such added absorption lines are given a fixed Doppler parameter  $b = 27 \text{ km s}^{-1}$ . For the *VLT* spectrum, multiple Gaussian profiles are often introduced to fit a single absorption feature. Fitting to the corresponding *FUSE* data sometimes converge to one of these profiles, but fails to identify the others. In such a case, we fix this set of profiles to the same  $\eta$  value, as these absorbers are ionized by the same radiation field. Approximately ten H I absorption lines have no apparent He II counterparts, and they are not apparently blended. We assign He II column densities to these lines as  $1\text{-}\sigma$  lower limits that are on the order of  $10^{13} \text{ cm}^{-2}$ , and mark them in Table 1 with null errors in the He II column density. Most of these absorption lines are only marginally detected in the *VLT* data; therefore their reality may be questionable. It is worth noting that uncertainties in the *FUSE* data reduction and fitting, particularly the imperfect background subtraction may contribute significant errors in these peculiar absorption lines.

At wavelengths shortward of 996 Å, the presence of He II Ly $\beta$  poses additional difficulty in line identification. We fit the *FUSE* data in this region in two ways. For lines that are not badly blended, we fit He II Ly $\alpha$  and Ly $\beta$  simultaneously, using the same approach we applied to the *VLT* H I spectrum. The Ly $\alpha$  and Ly $\beta$  lines are forced to have the same column density, redshift, and Doppler parameter. For those lines that are blended, the noisy Ly $\beta$  region can adversely affect the fitting process. In such cases, we determine the He II column densities of the Ly $\beta$  lines from the longer-wavelength Ly $\alpha$  lines alone and fix this parameter for the corresponding Ly $\beta$  line. We then fit the He II Ly $\alpha$  lines in the blended region using the corresponding H I lines from the *VLT* spectrum to fix the redshifts and line widths. As

above, if additional He II opacity is needed at specific wavelengths, we add additional He II Ly $\alpha$  components with a fixed Doppler parameter. We do not fit the spectrum below 920 Å, as blended Lyman-series airglow contamination becomes too strong to correct.

At wavelengths longward of 1000 Å, our fits agree well with those in Kriss et al. (2001), but require fewer added He II components. The higher quality of our *VLT* spectrum allows us to identify more weak hydrogen absorbers. Between 1000 and 1130 Å, we identify 362 absorption lines with both H I and He II Ly $\alpha$  absorption and only require 43 additional He II Ly $\alpha$  lines with no H I counterpart. The number of identified H I Ly $\alpha$  forest lines is nearly twice that in the *Keck* spectrum of this object (Songaila 1998; Kriss et al. 2001) over this spectral range, and they include most of the added He II Ly $\alpha$  components in the work of Kriss et al. (2001). The properties of sample components are listed in Table 1: their absorption redshifts, He II column densities, Doppler parameters, H I column densities, and  $\eta$  values. Null errors in the Doppler parameter represent an added component that is not detected in the *VLT* data (the corresponding H I column density is the upper limit.) In such a case, the  $\eta$  value is an upper limit.

## 4. DISCUSSION

### 4.1. Distribution of Absorption Features

The H I Ly $\alpha$  forest lines in quasar spectra follow a well-defined power-law distribution,  $dn/dN \propto N^{-\beta}$ , where  $\beta = 1.5$  at  $3 \times 10^{12} < N < 10^{15} \text{ cm}^{-2}$  (Tytler 1987; Rauch 1998; Kim et al. 2002). At higher column density there are more damped systems than this power law predicts. Below  $N < 3 \times 10^{12} \text{ cm}^{-2}$ , line identification becomes difficult, and the results are not certain. Hu et al. (1995) suggest that this power law may be extended to lower column density, assuming a large correction factor.

As the *FUSE* data reveal a large number of absorption lines with low H I column density, useful information about their distribution with column density may be obtained. We first examine the column-density distribution of the Ly $\alpha$  lines that are observed in both H I and He II. In Figure 2, the distribution of the H I forest lines in HE2347–4342 is plotted. The results are consistent with a power law of  $\beta = 1.5$  between  $3 \times 10^{12} < N < 10^{16} \text{ cm}^{-2}$ . Another histogram displays the distribution of values derived from the He II column density. Each data point is divided by 62, the median  $\eta$ . The distribution of these calculated hydrogen absorption lines follows a pattern similar to the real ones, demonstrating the possibility of using He II parameters to describe the H I counterparts. The histograms do not match well at higher column density, as a result of this simplified approach which assumes a fixed value

for  $\eta$ .

We extend the database for Figure 2 with additional absorption lines which are detected only in He II. If the average value of  $\eta = 300$ , approximately 100 data points are added to the He II database in Figure 2, to produce the results displayed in Figure 3. If we choose a value lower than 300, many absorption-lines should have been detected in the optical spectrum, and values higher than 300 will leave a gap in the distribution shown in Figure 3. The added points represent our estimate of the low-column-density end of the H I absorption line distribution. There is a significant downturn around  $N = 3 \times 10^{12} \text{ cm}^{-2}$ , from  $\beta \sim 1.5$  to 0.3. On the basis of this pattern, we infer that the number of absorption lines with  $N < 10^{11} \text{ cm}^{-2}$  is negligible.

A part of the observed trend in Figures 2 and 3 at the low-column-density end may be attributable to the confusion limit of the *FUSE* data: Weak absorption features fall into other troughs and become undetected. We have carried out simulations by introducing additional absorption lines into the *FUSE* spectrum, and performing the same line-fitting procedure described in §3. At a He II column density of  $\sim 10^{15} \text{ cm}^{-2}$ , more than 90% of the absorption lines are identified. At  $\sim 10^{14} \text{ cm}^{-2}$ , approximately two thirds of the lines are identified. The others are heavily blended, and the fitting task only yields a single fitted component for them. This may explain why many fitted lines have Doppler parameters greater than 40  $\text{km s}^{-1}$ . At the limiting column density of  $10^{13} \text{ cm}^{-2}$ , only one out of five may be detected. Assuming an average  $\eta = 300$ , these components have their H I column density on the order of  $10^{10} \text{ cm}^{-2}$ . A correction factor of 5 may therefore increase the number of weak absorbers at  $N < 10^{11} \text{ cm}^{-2}$ . The downturn of the distribution shown in Figure 3 takes place at a He II column density of  $N \sim 10^{15} \text{ cm}^{-2}$ , where the correction factor is insignificant. We therefore suggest that this change in the distribution is real, not just the result of confusion.

## 4.2. Velocity Field in the IGM

An important but as yet unknown parameter in the IGM is the velocity ratio  $\xi = b_{\text{He}}/b_{\text{H}}$  between the  $\text{He}^+$  ions and hydrogen atoms in an individual spectral feature. This is a vital clue to the actual physical processes that dominate the evolution of structure in the IGM. Previous models and observations often assumed a value, either 1.0 for purely turbulent motions, or 0.5 for purely thermal broadening, in order to constrain other parameters. Even with the high spectral resolution of *FUSE*, an attempt to derive the He II Doppler line widths is difficult because of line blending and the low S/N. In spectral voids, however, where absorption lines are sparse, we have identified a sample of individual He II and H I absorption lines that are not blended in either  $\text{Ly}\alpha$  or  $\text{Ly}\beta$ . We fit the profiles of these

individual absorption features (Figures 4 and 5) and let the velocity widths vary as free parameters. The optical depths of the  $\text{Ly}\alpha$  and  $\text{Ly}\beta$  lines are also linked by simple atomic physics, providing an important additional constraint on the allowed range of the fitted line widths. Table 2 summarizes the results of our fits. A linear fit to the line widths yields a ratio of the He II to H I line widths of  $\xi = 0.95 \pm 0.12$ . As shown Figure 6, this velocity ratio is consistent with turbulence being dominant, with one or two cases of possible thermal line broadening. We therefore have assumed identical He II and H I line widths for all absorption lines in our analysis.

### 4.3. Evolution of Ionization Level

The derived  $\eta$  ratios are plotted in Figure 7, along with the lower limits from those He II  $\text{Ly}\alpha$  lines which do not have H I counterparts (now a minor fraction of the data set,  $< 10\%$ ) and the upper limits from the H I lines without significant He II counterparts. Our analysis reveals a significant population of IGM structures with hydrogen column densities between  $5 \times 10^{11}$  and  $2 \times 10^{12} \text{ cm}^{-2}$ . They account for approximately 40% of all the identified He II absorption lines. We calculate the average value of  $\eta$  in logarithmic units, including only lines that are detected in both the *FUSE* and *VLT* spectra. For  $n$  data points, we calculate the logarithmic average as  $\log(\bar{\eta}) = (\sum \log(\eta_i))/n$ , and its corresponding uncertainty as  $\log(\Delta\bar{\eta}) = (\sum (\log(\Delta\eta_i))^2)^{1/2}/n$ . The average value of  $\eta \sim 48 \pm 10$  strongly suggests that the main ionization source is the accumulated emission from quasars. Zheng et al. (1997) and Telfer et al. (2002) derive a mean spectral index below  $1000 \text{ \AA}$  for quasars of  $\alpha \sim -1.7$ , which is consistent with the ionization level measured here. The median value of  $\eta$  is 62, which is reasonably close to the average value. However, there is significant variation of the ionization parameter  $\eta$ , from less than unity to over a thousand. Some lines with low  $\eta$  values in our list are associated with heavily saturated Lyman-limit systems, in which the measurement errors are large.

Cases with  $\eta > 500$  may represent the regions in the IGM that are ionized by local soft radiation sources, but not yet by the metagalactic UV background radiation field. Approximately 90 such lines are added in fitting the *FUSE* spectrum, particularly at  $z > 2.7$ . They are needed to explain the complete absorption troughs, and they confirm the suggestion of Zheng et al. (1998) that a significant part of the He II absorption may be produced by absorption lines without detected H I counterparts. These lines represent the tenuous regions of the IGM that have not been detected in hydrogen. The lack of such high  $\eta$  values at lower redshifts suggests that the ionization of intergalactic helium is fairly complete at  $z \sim 2$ .

Figures 7 and 8 show that the column-density ratio  $\eta$  decreases gradually toward lower

redshift. The main reason appears to be the decline in the number of absorption lines with  $\eta > 1000$  with decreasing redshift (only one is seen below  $z = 2.25$ ), as the He II reionization by a metagalactic UV background field becomes complete. Haardt and Madau (1996) and Madau et al. (1999) model the evolution of the ionizing continuum under the assumption that quasar emission is the dominant source of ionizing photons and suggest that the He II/H I ratio in the IGM and the Ly $\alpha$  clouds increases from  $\sim 25$  at  $z = 0$  to  $\sim 45$  at  $z = 2.5$ , and then decreases again below 30 for  $z > 4.5$ . Telfer et al. (2002) study the EUV continuum shape of quasars and find that it remains fairly constant between redshifts of 0.3 and 2. Such a trend is also noted in the model results of Fardal et al. (1998) for a fixed continuum-power-law index. Our results strongly suggest that the main ionizing source at redshift  $z \sim 2.8$  is the accumulated radiation from quasars.

As suggested by Kriss et al. (2001) and Shull et al. (2003), the large variations in  $\eta$  may be due to local sources of ionizing radiation. For each observed value of  $\eta$ , we infer the incident spectral index  $\alpha_{EUV}$  (defined by  $f_\nu \propto f^{-\alpha_{EUV}}$ ) using models of power-law radiation propagated through the IGM (Fardal et al. 1998, model A2 in their Figure 10). In Figure 9 we compare this distribution of inferred spectral indices to those measured by Telfer et al. (2002). At low values of  $\alpha_{EUV}$  the two distributions are similar, suggesting that the observed variations in  $\eta$  are consistent with the natural variation of intrinsic quasar spectral indices. At high values of  $\alpha_{EUV}$ , however, the excess of features with high  $\eta$  indicates a contribution from an additional population of soft ionizing sources such as star-forming galaxies or obscured AGN. One problem with this simple interpretation is that the observed space density of quasars at  $z = 2.5$  is too sparse to produce fluctuations on the observed scale of  $\Delta z = 0.001$ , and the expected high space density of star-forming galaxies should produce a more uniform radiation field. As discussed by Shull et al. (2003), the combination of the natural variation in quasar spectral indices, the resulting difference in the proximity spheres for H I and He II, and radiative transfer through a non-uniform IGM may all conspire to produce the observed variations in  $\eta$ .

#### 4.4. Evolution of He II Opacity

Studies of He II absorption along several lines of sight (Davidsen et al. 1996; Heap et al. 2000; Kriss et al. 2001, and references therein) have shown that from  $z = 2.3$  to  $z = 3.3$  the average opacity increases toward higher redshift. In our reprocessed *FUSE* spectrum of HE2347–4342, for a given section of the spectrum, we calculate the average transmission and its associated uncertainty by summing over the  $n$  data points  $\overline{T} = (\sum t_i)/n$  and  $\overline{\Delta T} = (\sum (\Delta t_i)^2)^{1/2}/n$ , where the transmission at each point  $i$  in the normalized binned

spectrum is given by  $t_i$ . The He II Ly $\alpha$  optical depth is then calculated as  $\tau_\alpha = -\ln \bar{T}$ . At wavelengths shorter than 995.5 Å, however, we must modify this procedure as He II Ly $\beta$  and other higher-order Lyman series lines begin to blend in with the He II Ly $\alpha$  forest. The high resolution of the *VLT* and *FUSE* spectra enable us to separate the Ly $\alpha$  absorption lines at  $z < 2.27$  from high-order Lyman lines at higher redshift. To isolate the contribution from the Ly $\alpha$  absorption lines alone, we construct a model for the short-wavelength section of the spectrum based on the H I line list from the fitted *VLT* spectrum (for the He II Ly $\alpha$  lines) and the fitted parameters of the longer-wavelength He II Ly $\alpha$  lines (for the higher-order Lyman lines). At wavelengths shortward of 995.5 Å ( $z < 2.28$ ), we then calculate the He II Ly $\alpha$  opacity from this modeled spectrum. Figure 10 shows the average He II Ly $\alpha$  optical depth as a function of redshift. For comparison, we show the empirical trend with redshift for He II of  $\tau \propto (1+z)^{3.5}$  (Fardal et al. 1998). At redshifts below 2.7, the agreement is quite reasonable; however, at higher redshift, the opacity grows much more rapidly. We discuss this in the next section.

#### 4.5. He II Opacity at $z > 2.7$

At redshifts above  $z = 2.7$ , the spectrum of HE2347–4342 is largely opaque in He II Ly $\alpha$ . The high S/N *HST*/STIS spectrum (Smette et al. 2002) shows several deep absorption troughs at  $z > 2.77$ . Following the nomenclature and wavelength intervals defined in their Table 3, Troughs A, C, D, and I have average He II Ly $\alpha$  optical depths of  $\sim 4$  or more. Our new short-wavelength *FUSE* data allow us to derive more accurate optical depths in these deepest troughs since we can now measure the opacity not only in Ly $\alpha$ , but also in the corresponding higher-order Lyman lines. For example, trough A is seen in Ly $\alpha$  (1175.6–1178 Å), Ly $\beta$  (991.8–993.8 Å), and Ly $\gamma$  (940.5–942.4 Å). Because of these low S/N and uncertain continuum, the Ly $\gamma$  troughs (visible in Figure 1) are not quantitatively useful in improving the limits on the Ly $\alpha$  opacity. To measure the average optical depth due to Ly $\beta$  alone in a given wavelength interval, we first calculate the optical depth directly from the *FUSE* spectrum. There are overlying He II Ly $\alpha$  lines throughout this region of the spectrum, however, and we correct for these by using the predicted He II Ly $\alpha$  opacity based on the H I Ly $\alpha$  line list in each of these intervals obtained from the *VLT* spectrum. For each H I Ly $\alpha$  line, we assume the median value of the He II–H I column-density ratio  $\eta = 62$ , compute the corresponding He II Ly $\alpha$  column density, and assume that it has the same redshift and velocity width as the H I feature. We then integrate this synthetic He II Ly $\alpha$  spectrum to obtain the contaminating contribution of He II Ly $\alpha$  to the opacity in each of the regions that we measure for the Ly $\beta$  transmission. Table 3 summarizes our opacity measurements for each of the wavelength regions identified by Smette et al. (2002). For each He II Ly $\alpha$

wavelength region in column 2, we give the redshift at the center of the region in column 3, the He II Ly $\alpha$  opacity measured from the *FUSE* spectrum in column 4, the He II Ly $\alpha$  opacity from the STIS spectrum in column 5, the raw He II Ly $\beta$  opacity from the corresponding interval in the short-wavelength portion of the *FUSE* spectrum in column 6, the corrected opacity of the Ly $\beta$  region for overlying He II Ly $\alpha$  lines in column 7, and the inferred He II Ly $\alpha$  opacity based on the corrected Ly $\beta$  opacity in column 8. We derive the inferred Ly $\alpha$  opacity based on the higher-order Lyman lines using the standard relationship between the optical depth and the oscillator strengths for lines in the Lyman series:

$$\frac{\tau(\text{Ly}\alpha)}{\tau(\text{Ly}\beta)} = \frac{f(\text{Ly}\alpha) \lambda(\text{Ly}\alpha)}{f(\text{Ly}\beta) \lambda(\text{Ly}\beta)},$$

where  $f(\text{Ly}\alpha) = 0.4162$  and  $f(\text{Ly}\beta) = 0.0791$  are the oscillator strengths.

For the deepest troughs where only lower limits on the opacity could be set using the STIS spectrum, we conclude that the average optical depth of Ly $\alpha$  is high, but finite, with a typical value of  $\tau_{\text{Ly}\alpha} \sim 5$ . As shown in Figure 10, the distribution of the He II Ly $\alpha$  optical depth follows a slowly rising empirical curve similar to that observed for the overall H I opacity, and suddenly increases at  $z \sim 2.85$ . Such a sudden change in the He II opacity may signal the late stages of the reionization of intergalactic He $^+$  at  $z \sim 3$ . An analogous phenomenon is also observed for intergalactic hydrogen at  $z \leq 6$  (Becker et al. 2000; Fan et al. 2002; White et al. 2003), where the H I opacity abruptly rises from  $\sim 3$  to  $> 10$ . The predicted increase at this epoch is more rapid than  $\tau \propto (1+z)^{3.5}$  (Fardal et al. 1998), and the merging of ionized bubbles should produce a huge discontinuity at some slightly higher redshift. Numerical simulations of H I reionization (Razoumov et al. 2002) illustrate this same effect. A slow rise in opacity with redshift that roughly follows a power law in  $(1+z)$  shows first a marked departure from the power law followed by a discontinuity of several orders of magnitude that corresponds to the epoch when all the Strömgren spheres began to merge. Our inferences from the HE2347–4342 spectrum are consistent with indirect evidence from H I line widths (Ricotti et al. 2000; Theuns et al. 2002) and H I Ly $\alpha$  forest opacity (Bernardi et al. 2003) suggesting that the He II reionization discontinuity occurred at  $z = 3.2 - 3.4$ , and that we are seeing only the final stages in the process of He II reionization.

## 5. Summary

We have studied absorption by He II and H I in the IGM over a redshift range  $2.0 < z < 2.9$  using deep, new *VLT*/UVES spectra and reprocessed *FUSE* data for the quasar HE2347–4342. The *VLT* data reach a limiting H I column density of  $5 \times 10^{11} \text{ cm}^{-2}$ . More than 90% of the He II absorption lines identified in the *FUSE* spectrum have H I counterparts, suggesting

that we have traced most of the IGM mass, and that only a small fraction of it exists in regions with H I column density smaller than  $5 \times 10^{11} \text{ cm}^{-2}$ . The reprocessed *FUSE* data extend our view of He II absorption to wavelengths shortward of  $1000 \text{ \AA}$ , allowing us to study its properties down to redshifts as low as  $z \sim 2$ , and giving us access to the Ly $\beta$  portion of the forest. Using these data, we reach the following conclusions:

1. The distribution function of the absorption features is a power law with respect to hydrogen column density. The identified and added He II absorption lines in the *FUSE* spectrum suggest a low-column-density cutoff around an H I column density of  $3 \times 10^{12} \text{ cm}^{-2}$ , with a gradually diminishing contribution from lower column density features down to  $\sim 10^{11} \text{ cm}^{-2}$ .
2. By analyzing a sample of isolated He II features with both Ly $\alpha$  and Ly $\beta$  components, we are able to compare the He II line widths to the widths of their H I counterparts. We find that the ratio of He II to H I Doppler parameters  $\xi = b_{\text{He}}/b_{\text{H}} = 0.95 \pm 0.12$ , indicating that the IGM may be dominated by turbulent gas motions.
3. We find that the ratio of He II to H I column densities  $\eta$  shows a gradual evolution with redshift, decreasing from a median value of  $\sim 70$  at  $z = 2.85$  to  $\sim 40$  at  $z = 2.05$ . The number of He II absorption features with no H I counterparts, indicative of IGM regions photoionized by very soft spectra, also decreases with decreasing redshift (Figure 7 and 8). This trend suggests that by a redshift of 2, the ionization of intergalactic He $^+$  is mainly due to AGN.
4. From  $z = 2.0$  to  $2.7$ , we see a slow increase in He II Ly $\alpha$  optical depth. At  $z \sim 2$ , the average He II optical depth is about 0.5, increasing to  $\tau \sim 1$  at  $z \sim 2.6$ . A sudden increase in optical depth to  $\tau \sim 5$  is observed at  $z \sim 2.87$ . This trend in optical depth with redshift is analogous to that observed in H I at higher redshift.
5. We limit the He II Ly $\alpha$  optical depths in the opaque regions of the UV spectrum at  $z > 2.7$  to values of  $\tau_{\text{Ly}\alpha} \sim 5$  by using the corresponding troughs in the Ly $\beta$  portions of the spectrum to extend our dynamic range. This sudden, but finite, increase in optical depth suggests that we are seeing the end of the He II reionization process that began at an earlier epoch as indicated indirectly by the increase in H I line widths and H I opacity observed at  $z = 3.2 - 3.4$ .

The successful execution of the *FUSE* observations of this quasar is the result of many years of collaborative work of the *FUSE* science team. W.Z. would like to thank the staff at ESO Paranal observatory, especially Andreas Kaufer, for their professional help.



This work is based on data obtained for the Guaranteed Time Team by the NASA-CNES-CSA *FUSE* mission operated by the Johns Hopkins University. Financial support to U. S. participants has been provided by NASA contract NAS5-32985. A portion of this work is based on observations with the NASA/ESA *Hubble Space Telescope*, obtained at the Space Telescope Science Institute, which is operated by the Association of Universities for Research in Astronomy, Inc., under NASA contract NAS5-26555.

## REFERENCES

- Anderson, S. F., Hogan, C. J., and Williams, B. F. 1999, *AJ*, 117, 56
- Becker, R. H., et al., 2001, *AJ*, 122, 2850
- Bernardi, M., et al. 2003, *AJ*, 125, 32
- Bi, H., and Davidsen, A. F. 1997, *ApJ*, 479, 523
- Cen, R. 2003, *ApJ*, 591, 12
- Croft, R. A. C., Weinberg, D. H., Katz, N., and Hernquist, L. 1997 *ApJ*, 488, 532
- Davidsen, A. F., Kriss, G. A., and Zheng, W. 1996, *Nature* 380, 47
- Fan, X., et al. 2002, *AJ*, 12, 1247
- Fardal, M. A., Giroux, M. L., and Shull, J. M. 1998, *AJ*, 115, 2206
- Feldman, P. D., Sahnow, D. J., Kruk, J. W., Murphy, E. M., and Moos, H. W. 2000, *J. Geophys. Research*, 106, 8119
- FUSE* Observer’s Guide 2003, <http://fuse.pha.jhu.edu/support/guide/guide.html#INBKG>
- Haardt, F., and Madau, P. 1996, *ApJ*, 461, 20
- Heap, S. R., et al. 2000, *ApJ*, 534, 69
- Hogan, C. J., Anderson, S. F., and Rugers, M. H. 1997, *AJ*, 113, 1495
- Hu, E. M., Kim, T.-S., Cowie, L. L., Songaila, A., and Rauch, M. 1995, 110, 1526
- Jakobsen, P., et al. 1994, *Nature*, 370, 35
- Kim, T.-S., Carswell, R. F., Cristiani, S., D’Odorico, S., and Giallongo, E. 2002, *MNRAS*, 335, 555
- Kriss, G. A. 1994, in *ASP Conf. Series 61: Astronomical Data Analysis Software and Systems III*, eds. D. R. Crabtree, R. J. Hanisch, and J. Barnes, (San Francisco: ASP), 437
- Kriss, G. A., et al. 2001, *Science*, 293, 1112
- Loeb, A., and Barkana, R. 2001, *ARAA*, 39, 19
- Madau, P., Haardt, F., and Rees, M. J. 1999, *ApJ*, 514, 648

- Miralda-Escudé, J., Cen, R., Ostriker, J. P., and Rauch, M. 1996 ApJ, 471, 582
- Moos, H. W., et al. 2000 ApJ, 538, L1
- Press, W., Rybicki, G., and Schneider, D. P. 1993, ApJ, 414, 64
- Rauch, M. 1998, ARAA, 36, 267
- Razoumov, A. O., Norman, M. L., Abel, T., and Scott, D. 2002, ApJ, 572, 695
- Reimers, D., Köhler, S., Wisotzki, L., Groote, D., Rodriguez-Pascual, P., and Wamsteker, W. 1997, A&A, 327, 890
- Ricotti, M., Gnedin, N. Y., and Shull, J. M. 2000, ApJ, 534, 41
- Sahnow, D., et al. 2000 ApJ, 538, L7
- Shull, J. M., Tumlinson, J., Giroux, M. L., Kriss, G. A., and Reimers, D. 2003, ApJ, in press
- Smette, A., Heap, S. R., Williger, G. M., Tripp, T. M., Jenkins, E. B., and Songaila, A. 2002, ApJ, 564, 542
- Songaila, A., 1998, AJ, 115, 2184
- Spergel, D. N., et al. 2003, ApJS, 148, 175
- Telfer, R. C., Zheng, W., Kriss, G. A., and Davidsen, A. F. 2002, ApJ, 565, 773
- Theuns, T., Bernardi, M., Prieman, J., Hewett, P., Schaye, J., Sheth, R. K., and Subbarao, M. 2002, ApJ, 574, L111
- Tytler, D. 1987, ApJ, 321, 49
- Venkatesan, A., Tumlinson, J., and Shull, J. M. 2003, ApJ, 584, 621
- White, R. L., Becker, R. H., Fan, X., and Strauss, M. A. 2003, AJ, 126, 1
- Wyithe, J. S. B., and Loeb, A. 2003, ApJ, 586, 693
- Zhang, Y., Anninos, P., and Norman, M. L. 1995, ApJ, 453, L57
- Zheng, W., Davidsen, A. F., and Kriss, G. A. 1998, ApJ, 115, 391
- Zheng, W., Kriss, G. A., Telfer, R. C., Grimes, J. P. and Davidsen, A. F. 1997, ApJ, 475, 469

Zheng, W., et al. 2004, AJ, in press (astro-ph/0311307)

### Figure Captions

Fig. 1.— Normalized spectra of quasar HE2347–4342. The upper panel shows the *FUSE* data, and lower panel the *VLT*/UVES data. Both the *FUSE* and *VLT* data are binned to 0.1 Å. The propagated errors are plotted as dashed curves. For the *FUSE* data, the errors are scaled down by a factor of 5 for clearer presentation, and are plotted only for positive data points. Strong airglow lines are removed and marked with an Earth symbol. Three spectral regions, where the He II opacity is significantly lower than average, are marked as B, F, G (after Smette et al.) and K, respectively. Seven regions of high He II opacity, defined by Smette et al., are also marked. The positions of Ly $\alpha$ , Ly $\beta$  and Ly $\gamma$  are indicated at the quasar redshift, and the wavelengths of the interstellar Lyman-series lines below 950 Å are labeled.

Fig. 2.— Column-density distribution of Ly $\alpha$  forest lines. The dashed line represents the expected values for a power law  $dn/dN \propto N^{-1.5}$ . The area marked with “He” represents the values that are derived from their He II column density, divided by the median  $\eta$  value of 62.

Fig. 3.— Column-density distribution of absorption systems, with added components that are detected via only He II absorption in the *FUSE* spectrum. To convert from He II column density to H I for these added components in the *FUSE* spectrum, we assume  $\eta = 300$  (marked by the scale at the top). Correcting for the confusion limit may increase the actual number of systems with column density  $N \lesssim 10^{11} \text{ cm}^{-2}$ .

Fig. 4.— Spectral features in void regions F and G. The *FUSE* data are binned to 0.05 Å. The arrows represent the identified absorption components. The Ly $\beta$  regions are blended with a number of prominent Ly $\alpha$  absorption features at  $z \sim 2.22$ , some of which coincide with the expected Ly $\beta$  features.

Fig. 5.— Spectral features in void region K. The *FUSE* data are binned to 0.05 Å. Some unmarked absorption features in the Ly $\beta$  regions are Ly $\alpha$  features at  $z \sim 2.14$ .

Fig. 6.— Doppler parameters for hydrogen and helium absorbers. The solid line is for expected values with turbulence line-broadening, and the dashed line for thermal broadening.

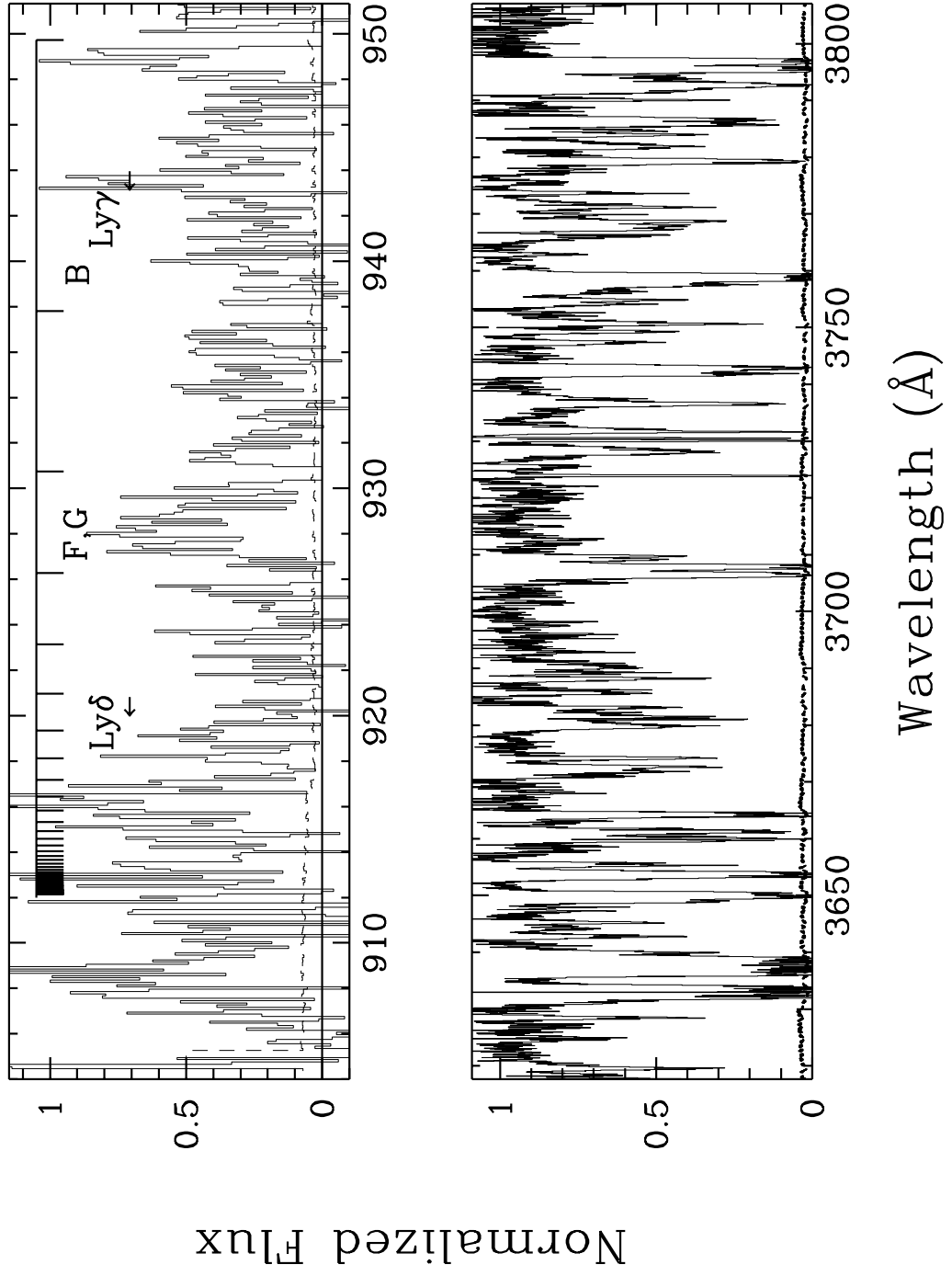
Fig. 7.— Column-density ratio  $\eta = N(\text{He II})/N(\text{H I})$  vs. redshift. The circles and upward arrows (colored red in the electronic edition) represent He II Ly $\alpha$  features that have no H<sup>0</sup> counterparts in the *VLT* spectrum and thus yield only lower limits to the indicated  $\eta$  ratios. The cross and downward arrows (colored blue in the electronic edition) represent H I

Ly $\alpha$  features that have no He II counterparts in the *FUSE* spectrum and thus yield only upper limits to the indicated  $\eta$  ratios. These  $\eta$  values are likely underestimated because of the limited *FUSE* data quality. At  $z < 2.28$ , above which higher-order He II Lyman lines become visible,  $\eta$  values from only the Ly $\alpha$  components are shown. The dashed curve represents the anticipated values if the ionizing sources are quasars with an EUV power law of  $f_\nu \propto \nu^{-1.76}$ , which are interpolated from the model results of Fardal et al. (1998).

Fig. 8.— Column-density ratio  $\eta$  vs. redshift. The average  $\eta$  value is calculated from the components that are detected in both the *FUSE* and *VLT* spectra. The dashed curve represents the anticipated values if the ionizing sources are quasars with an EUV power law of  $f_\nu \propto \nu^{-1.7}$ , which are interpolated from results of Fardal et al. (1998).

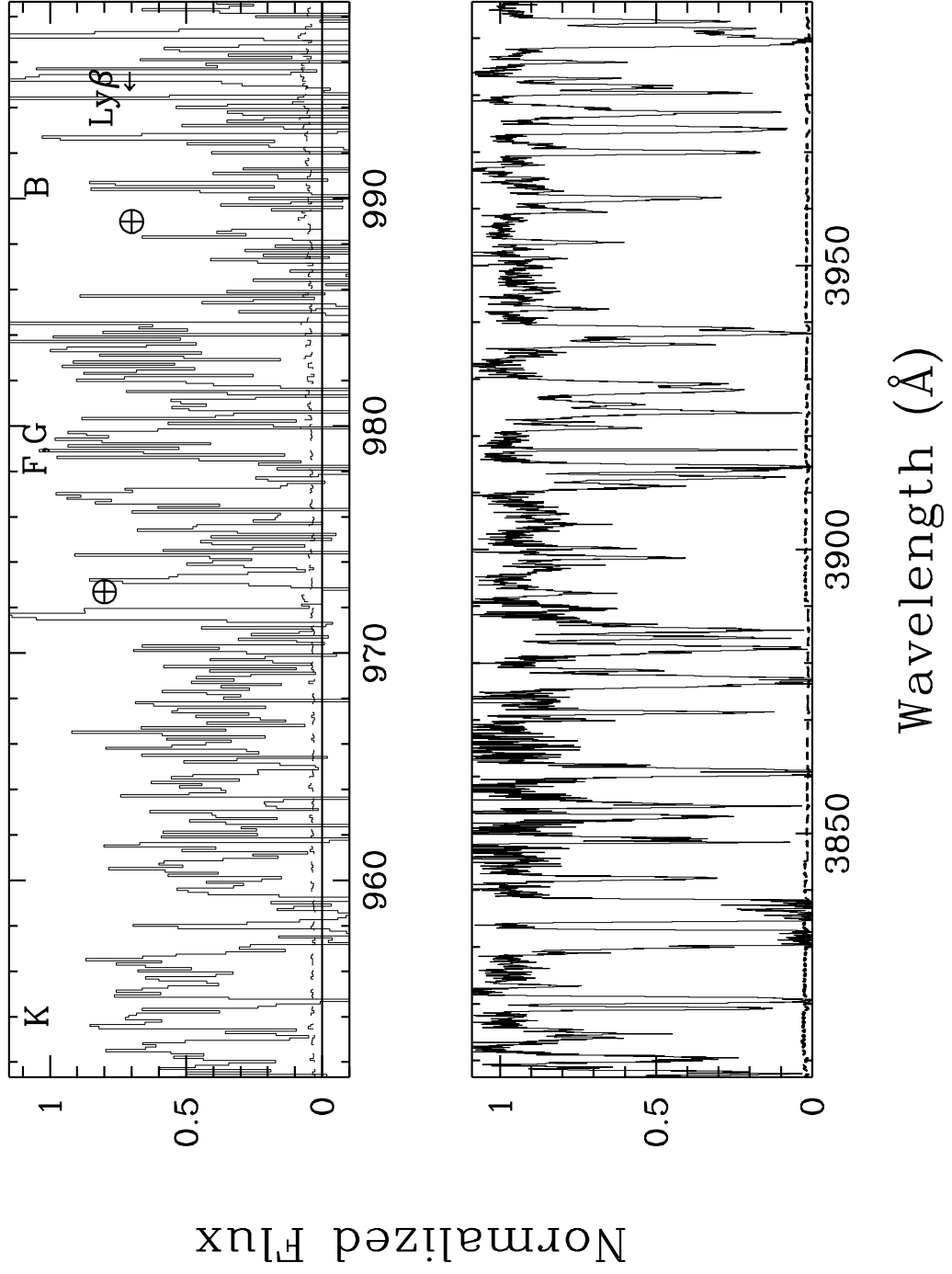
Fig. 9.— Distribution of power-law indices of the ionizing sources. The dashed line represents a scaled distribution of the  $\alpha_{EUV}$  of 39 radio quiet quasars (Telfer et al. 2002). The conversion from  $\eta$  to an inferred value for  $\alpha_{EUV}$  uses the quasar models of Fardal et al. (1998). The number excess at higher values indicates a contribution from soft ionizing sources such as star-forming galaxies or obscured AGN.

Fig. 10.— Redshift dependence of the He II Ly $\alpha$  opacity. Values below  $z = 2.3$  are derived from a line spectrum reconstructed from the fitted parameters that omit Ly $\beta$  and higher-order Lyman lines. Between  $z = 2.3$  and 2.7 the values are direct measurements from the *FUSE* data, and at  $z > 2.7$  they are derived from the observed He II Ly $\beta$  absorption region. The curve representing  $\tau \propto (1 + z)^{3.5}$  is plotted for comparison.



1a

Fig. 1.— a



1b

Fig. 1.— b



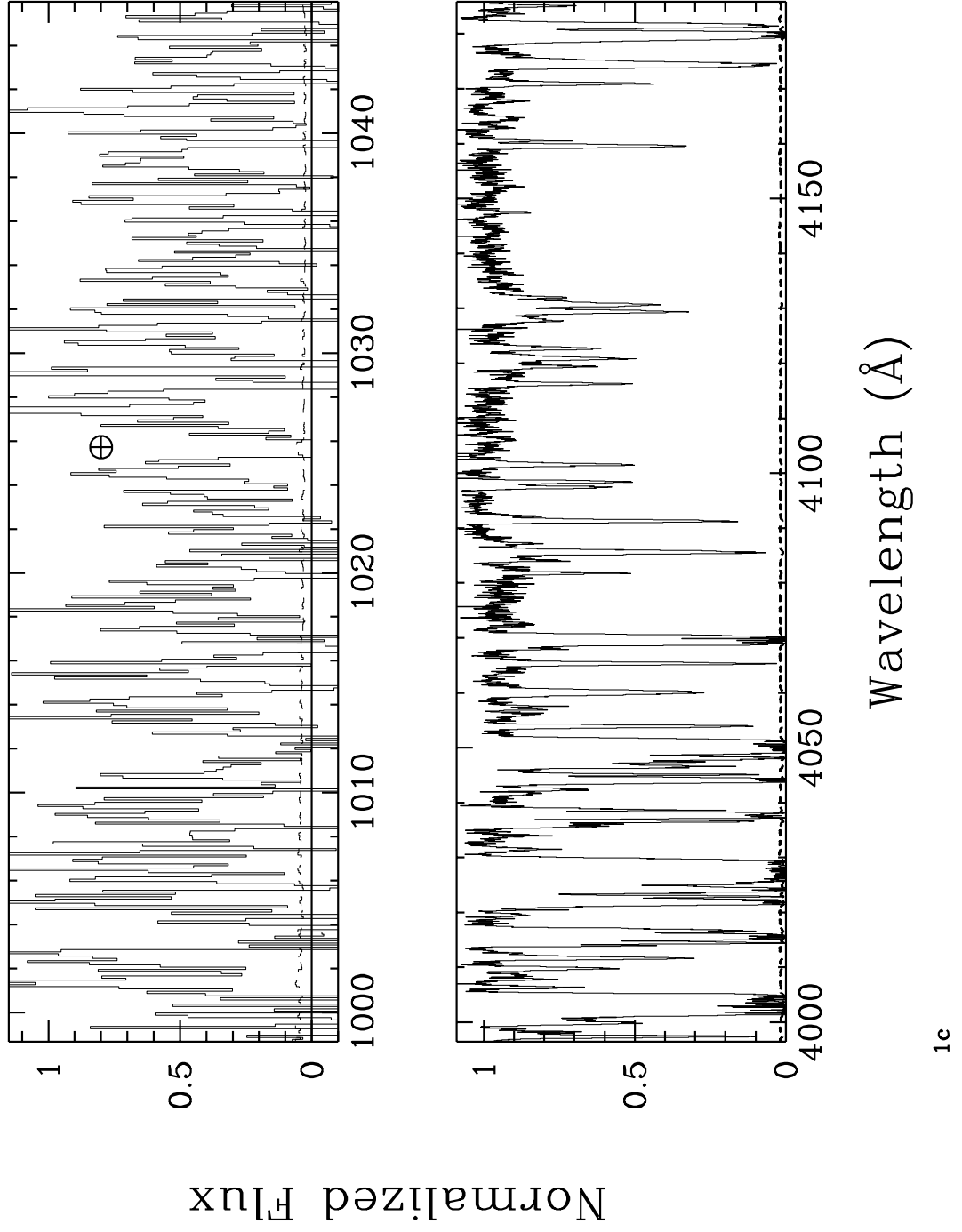


Fig. 1.— c

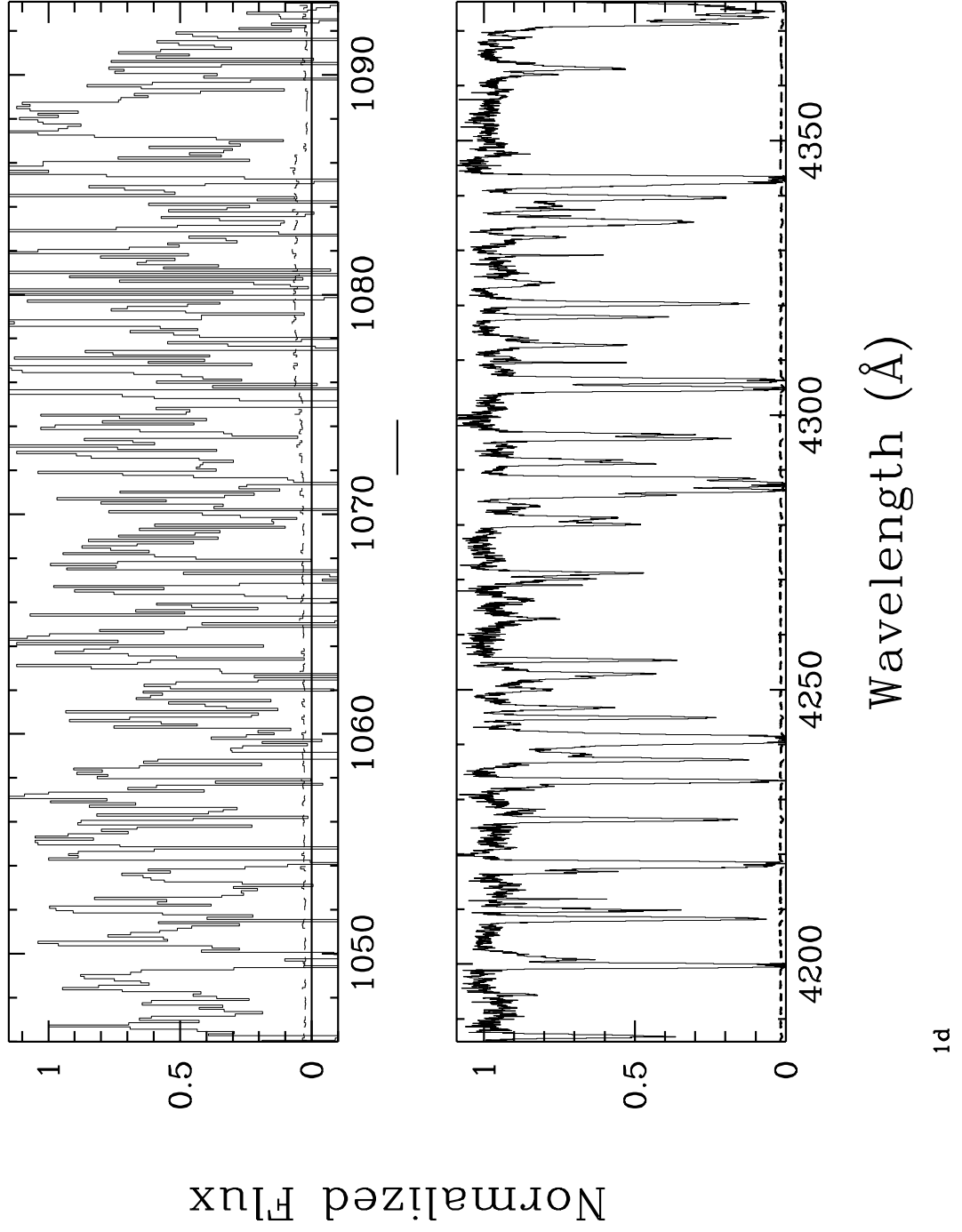


Fig. 1.— d

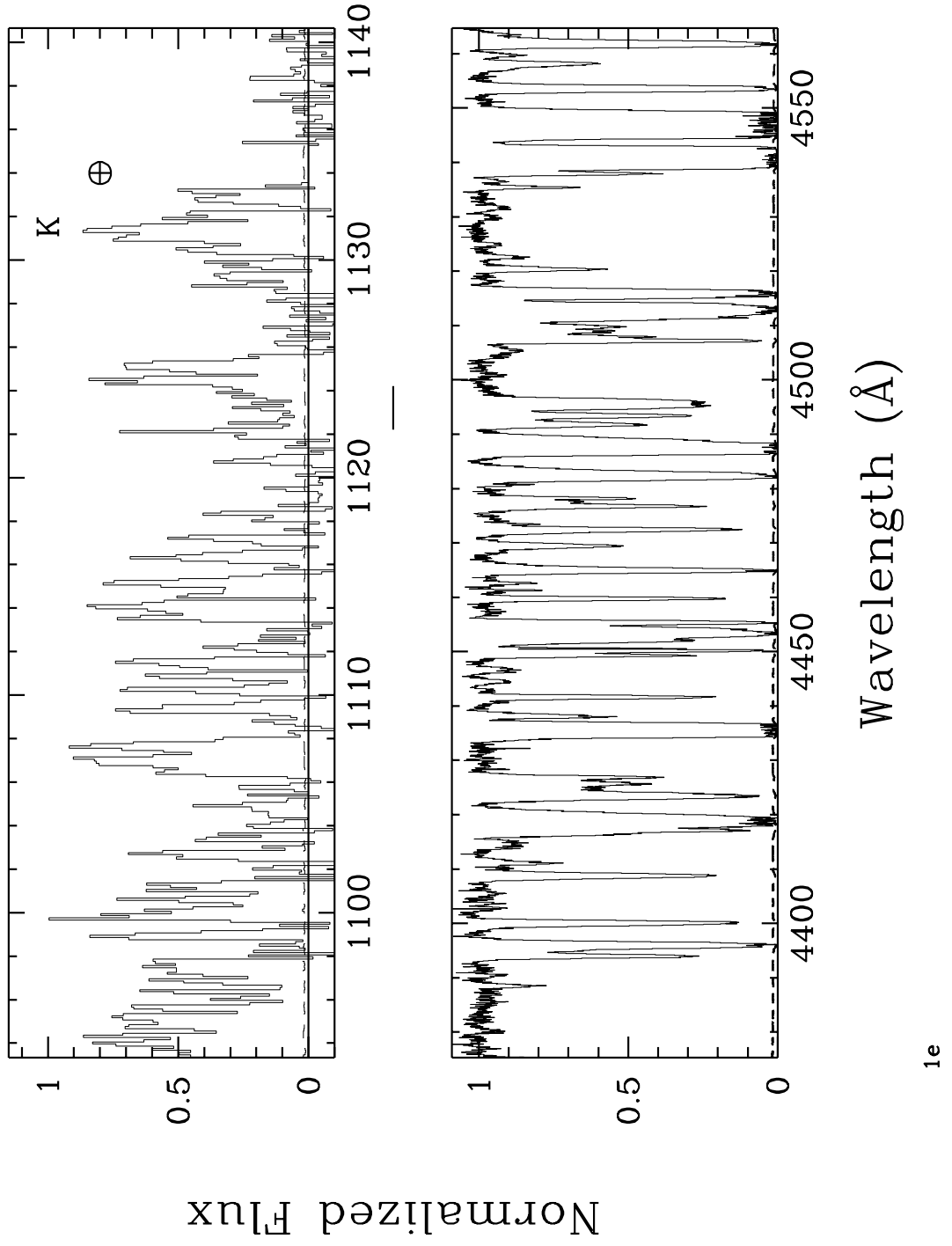
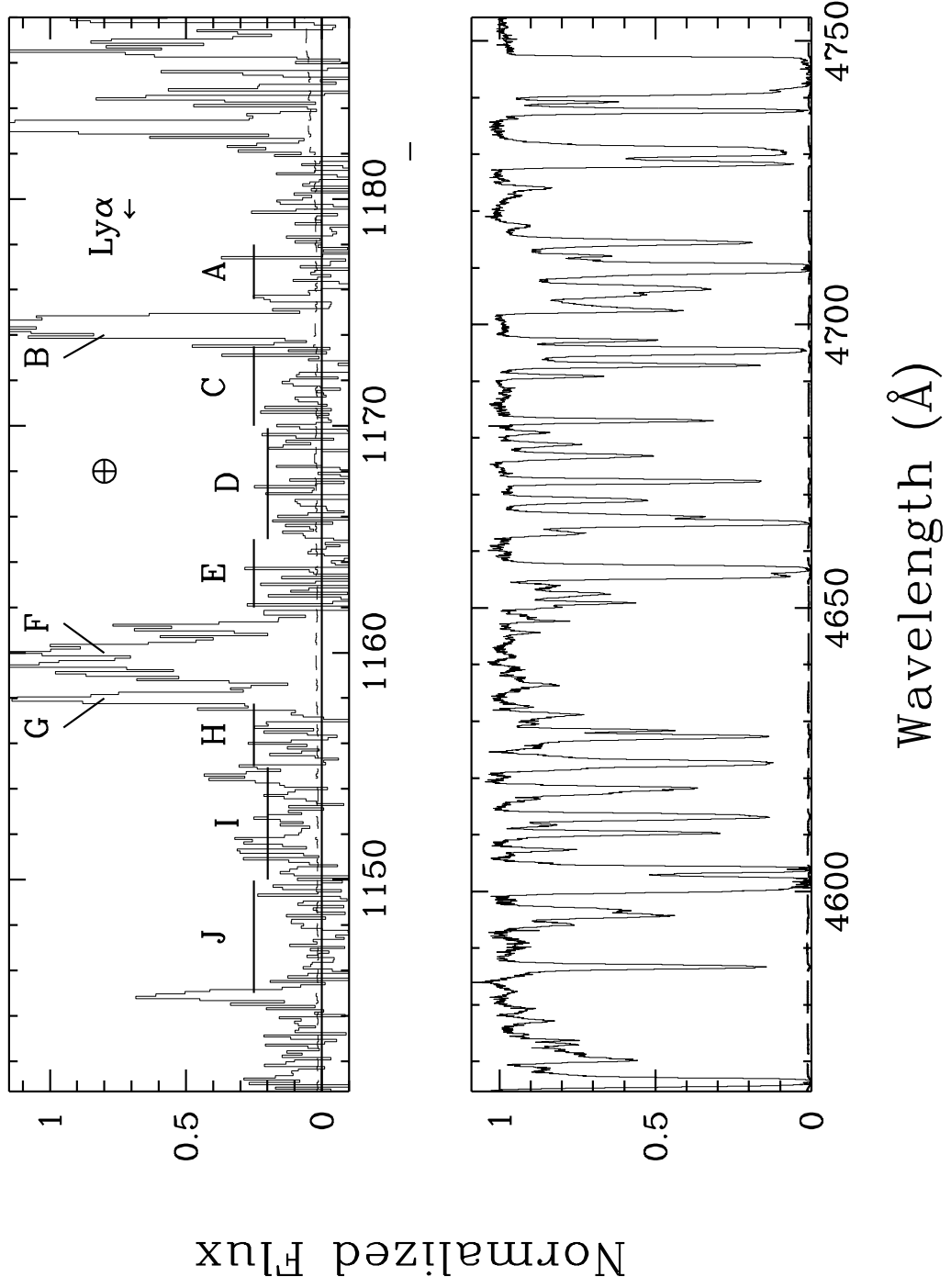


Fig. 1.— e



1f

Fig. 1.— f

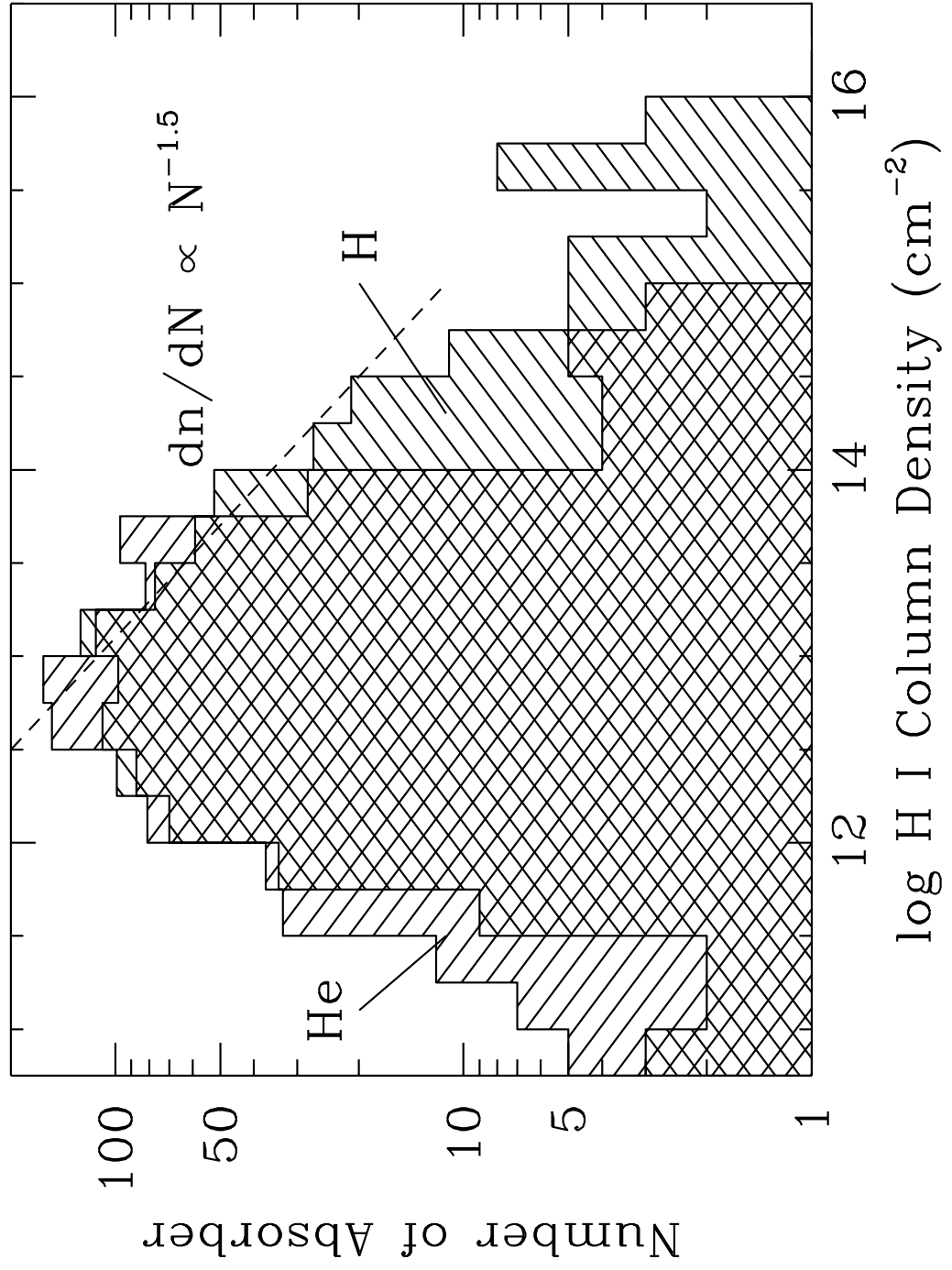


Fig. 2.—

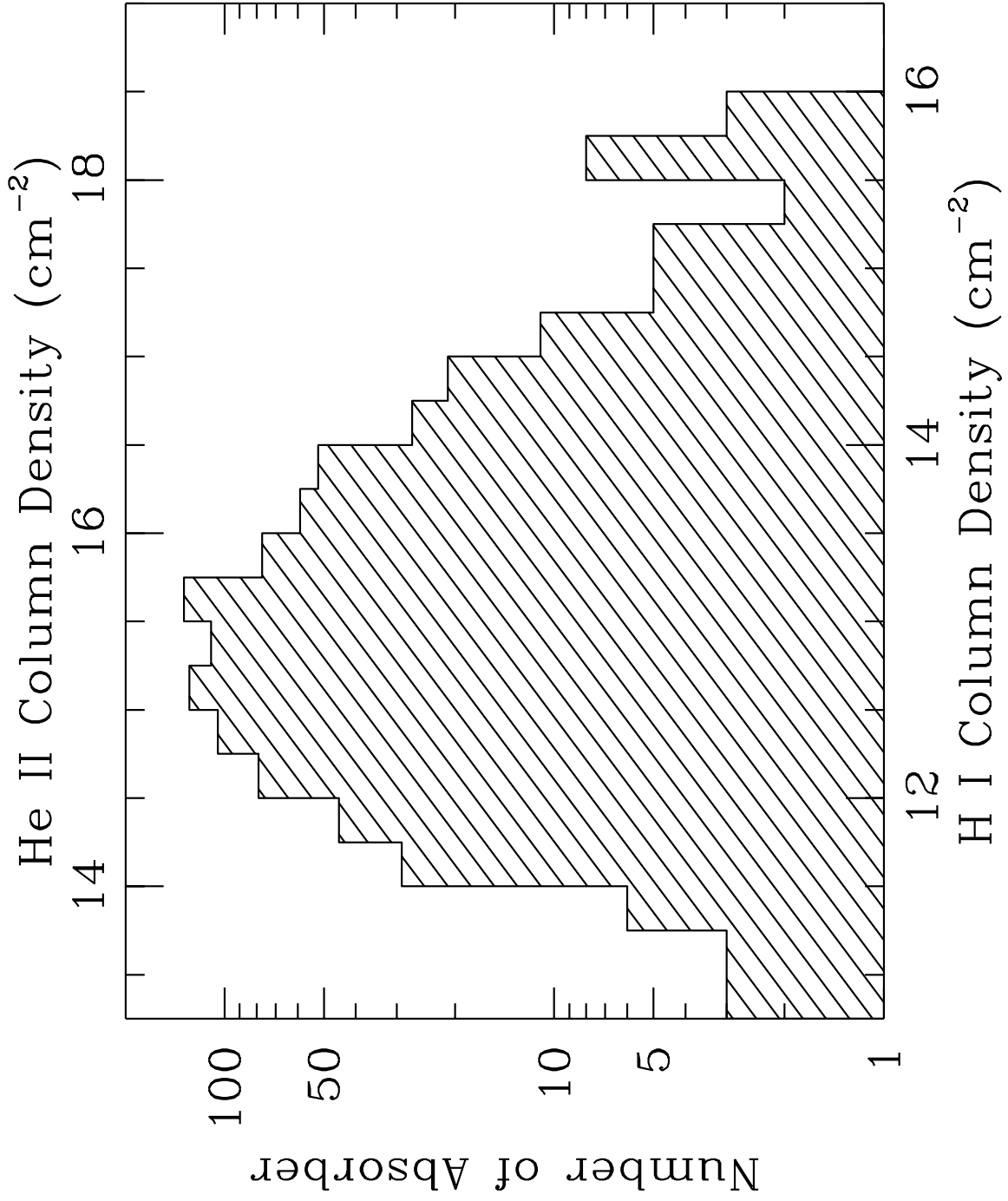


Fig. 3.—

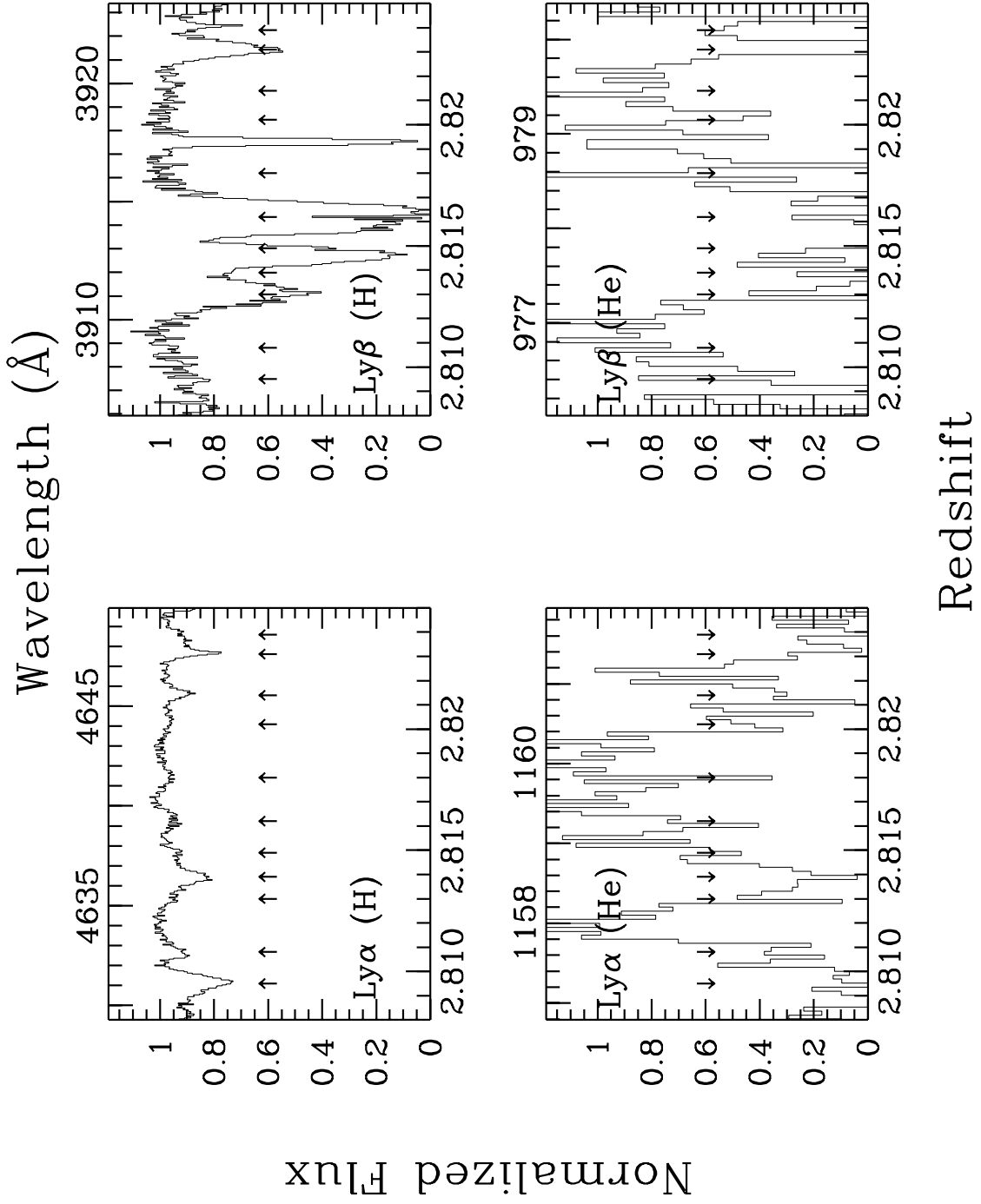


Fig. 4.—

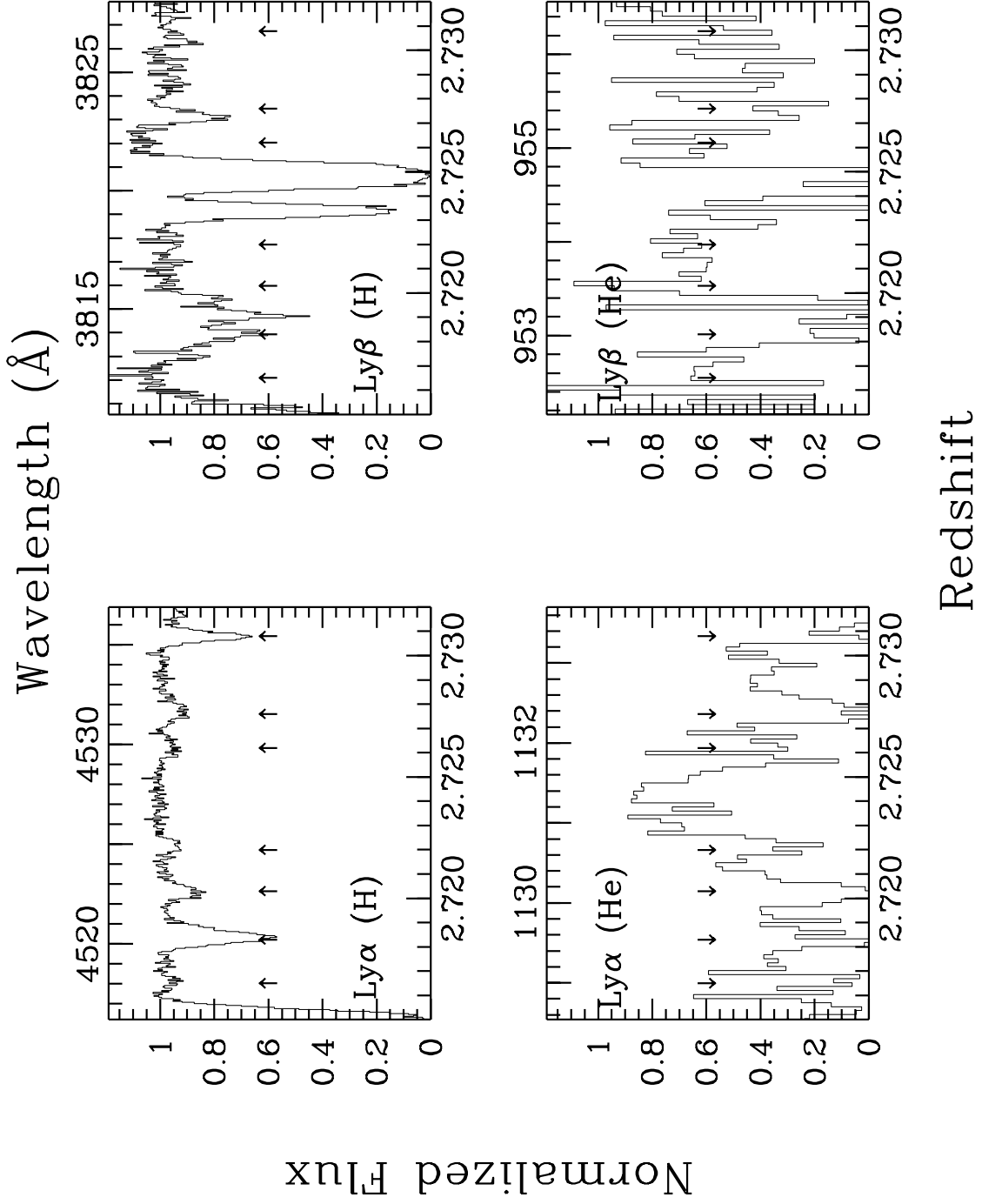


Fig. 5.—



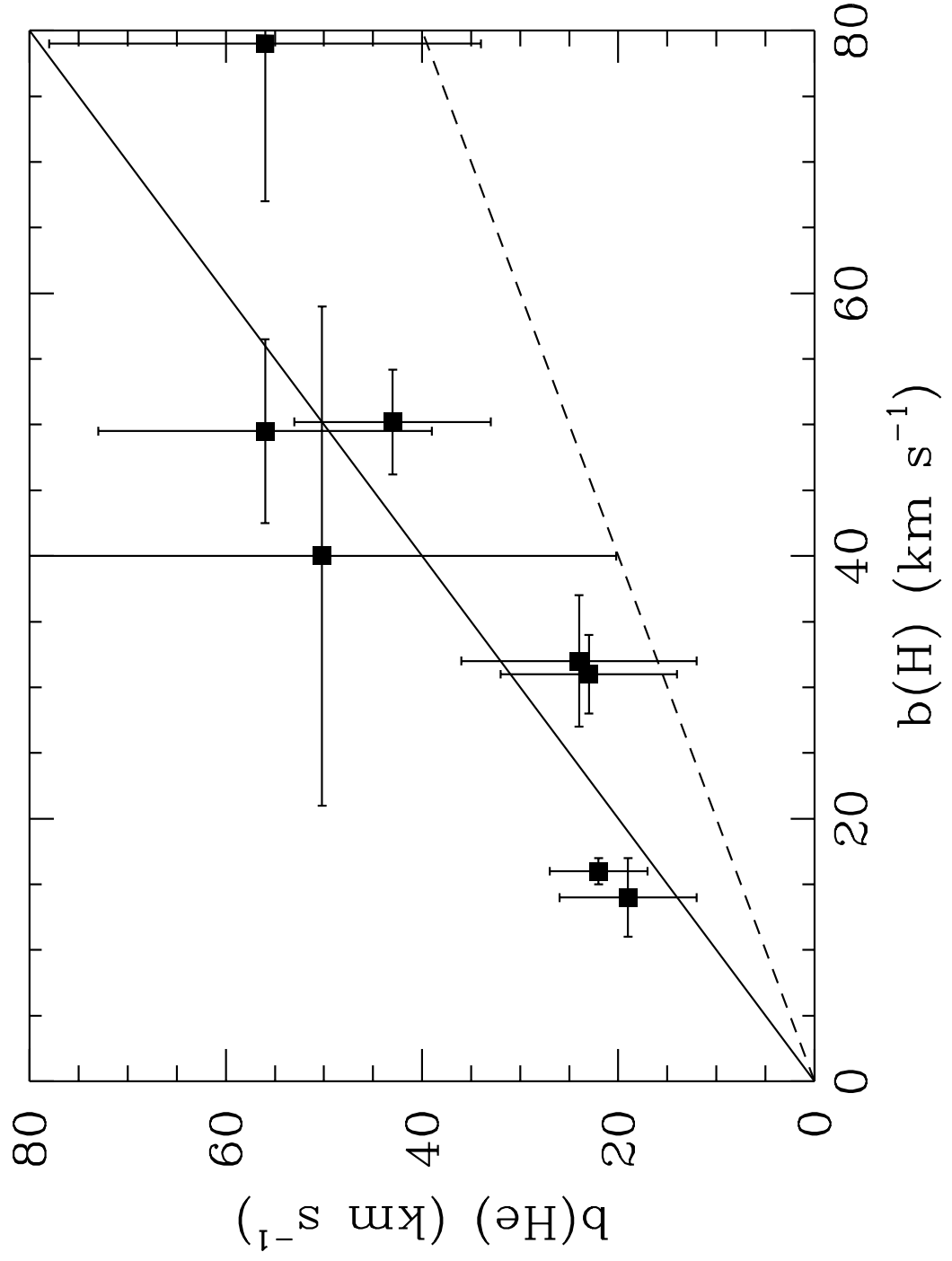


Fig. 6.—

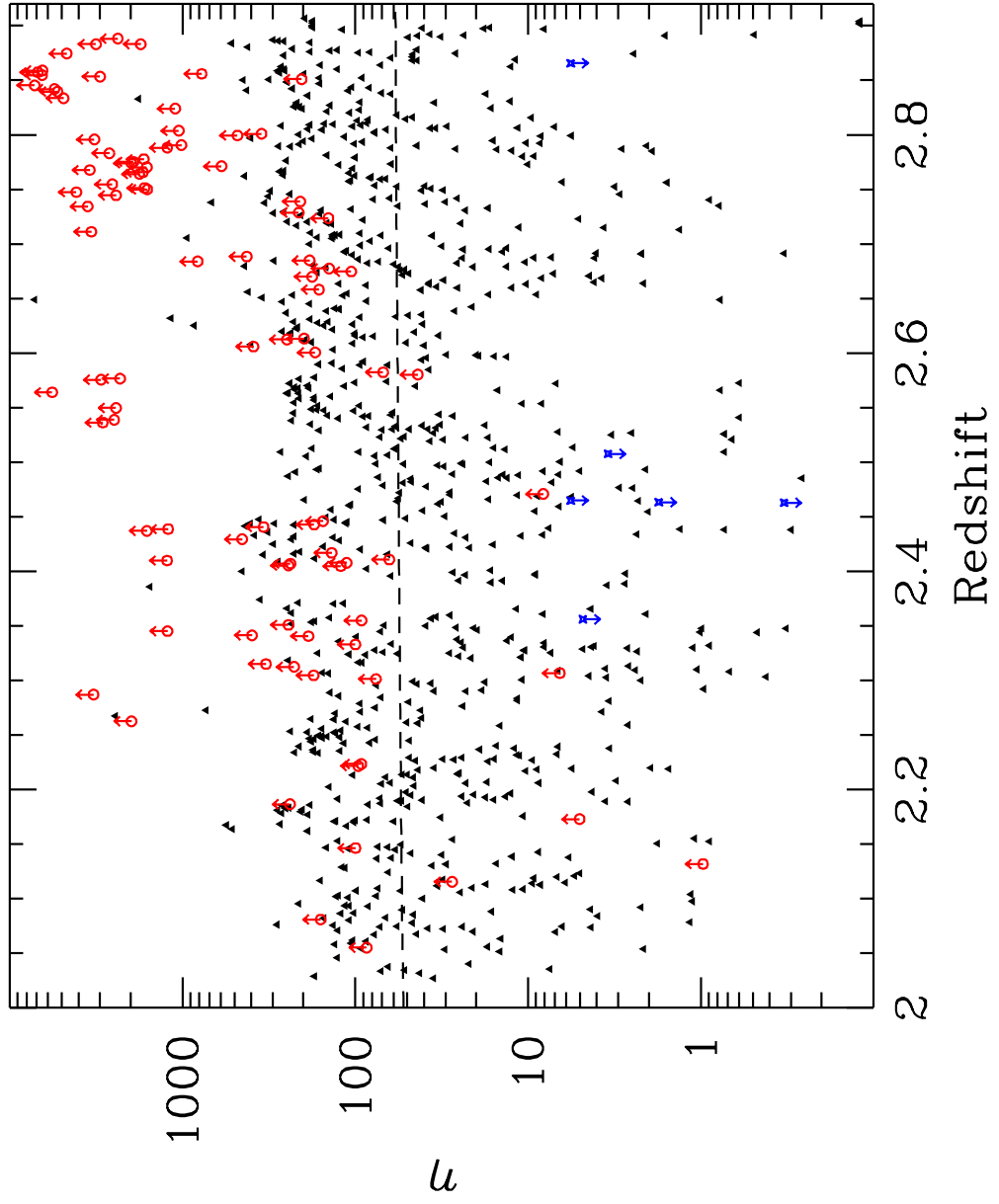


Fig. 7.—

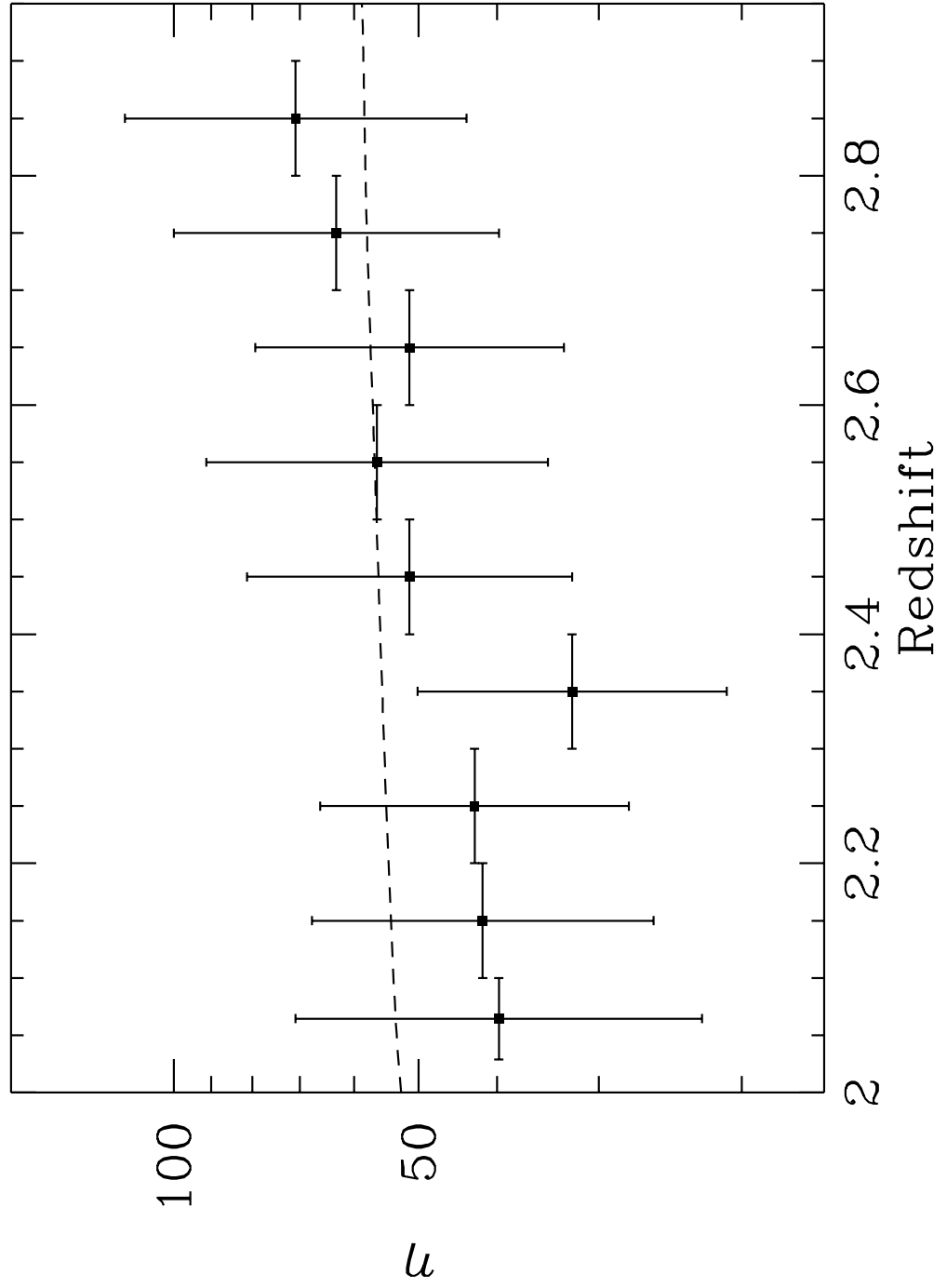


Fig. 8.—

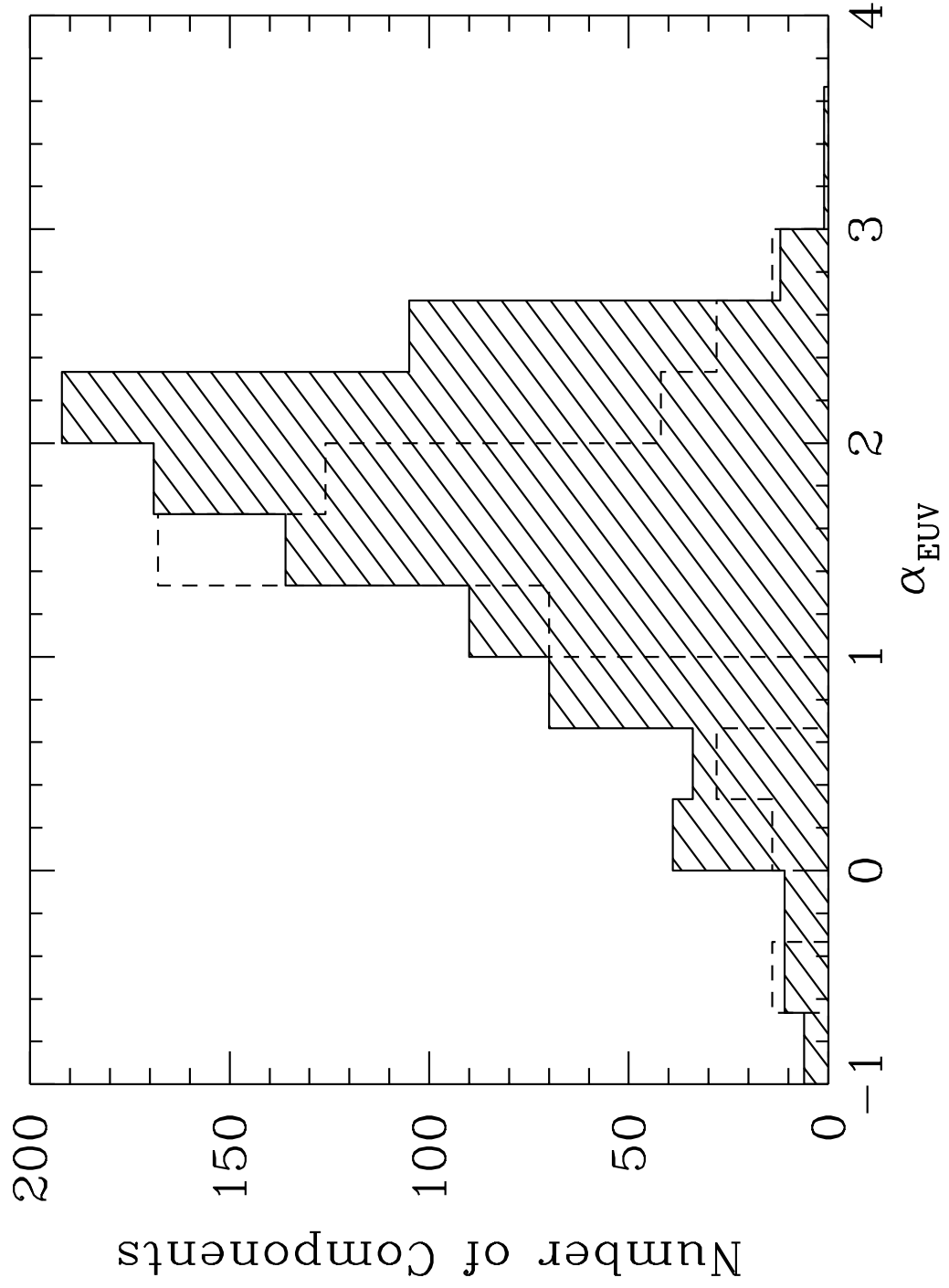


Fig. 9.—

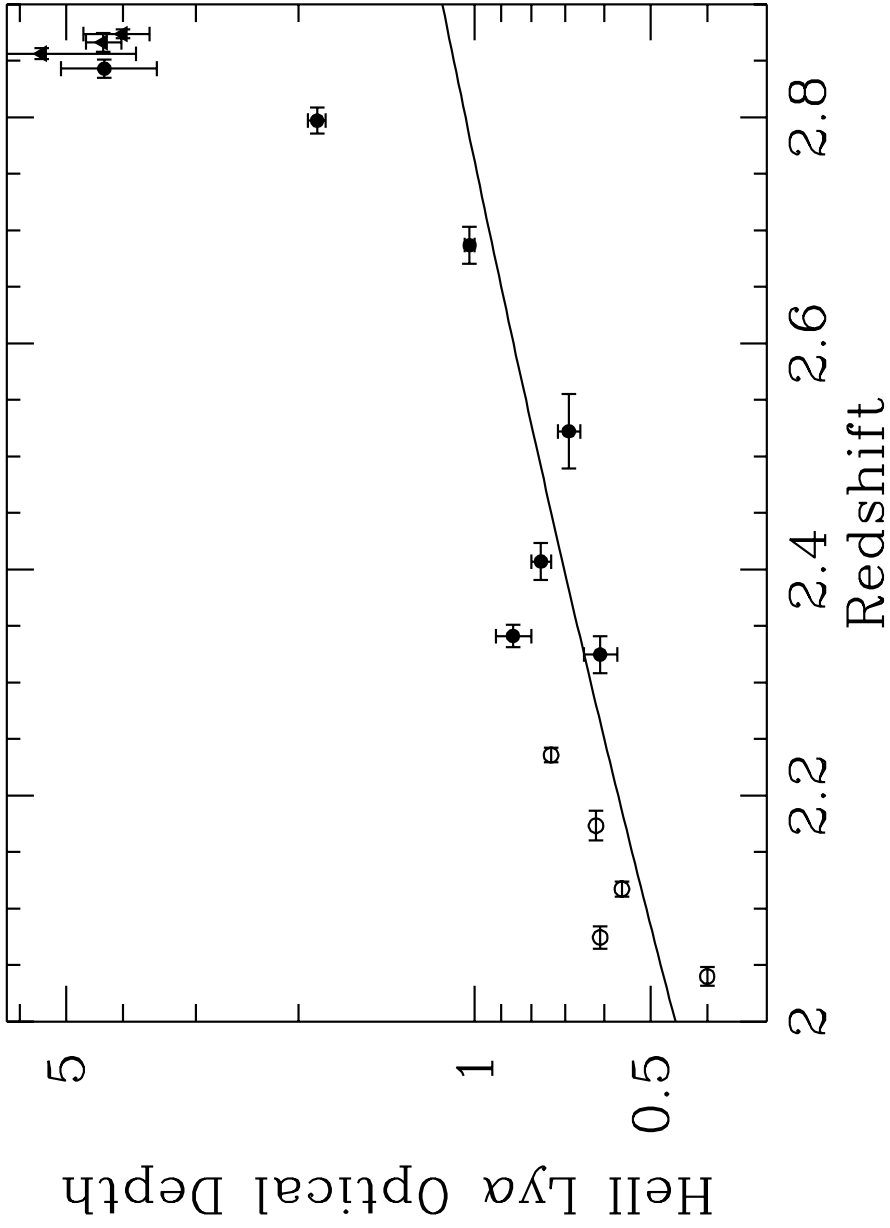


Fig. 10.—

Table 1. Properties of Fitted Absorption Components<sup>a</sup>

Redshift	N(He II) 10 <sup>12</sup> cm <sup>-2</sup>	b <sup>b</sup> km s <sup>-1</sup>	N(H I) 10 <sup>12</sup> cm <sup>-2</sup>	$\eta$
2.8881 ± 0.0002	1173 ± 228	27.0 ± 0.0	0.496 ± 0.000	2367
2.8872 ± 0.0009	616 ± 242	26.2 ± 67.4	2.05 ± 3.73	300
2.8861 ± 0.0001	914 ± 1040	22.1 ± 3.20	3.27 ± 1.96	280
2.8858 ± 0.0001	1019 ± 1706	30.3 ± 13.6	3.92 ± 2.15	260
2.8848 ± 0.0001	477 ± 958	30.4 ± 18.6	2.61 ± 1.40	182
2.8839 ± 0.0003	442 ± 3595	24.7 ± 46.1	0.849 ± 1.31	520
2.8831 ± 0.0002	1592 ± 17923	27.0 ± 0.0	0.502 ± 0.000	3172
2.8805 ± 0.0000	1175 ± 1456	19.8 ± 3.40	2.80 ± 0.653	420
2.8788 ± 0.0001	259 ± 5190	17.7 ± 6.30	1.12 ± 0.131	231
2.8781 ± 0.0000	2918 ± 7125	32.3 ± 0.500	66.3 ± 0.784	44.0

<sup>a</sup>The complete version of this table is in the electronic edition of the Journal. The printed edition contains only a sample.

<sup>b</sup>Zero error designates an added component with fixed value

Table 2. Absorption Lines in Spectral Voids

Redshift	N(He II) ( $10^{12} \text{ cm}^{-2}$ )	N(H I)	b(He II) ( $\text{km s}^{-1}$ )	b(H I)	$\eta$
2.8230	$374 \pm 100$	$3.9 \pm 0.4$	$22 \pm 5$	$16 \pm 1$	$95 \pm 26$
2.8214	$220 \pm 22$	$1.5 \pm 0.3$	$19 \pm 7$	$14 \pm 3$	$146 \pm 55$
2.8180	$112 \pm 42$	$2.0 \pm 0.3$	$24 \pm 12$	$32 \pm 5$	$57 \pm 24$
2.8161	$117 \pm 61$	$2.5 \pm 0.3$	$23 \pm 9$	$31 \pm 3$	$47 \pm 25$
2.7276	$777 \pm 616$	$4.8 \pm 1.1$	$88 \pm 66$	$50 \pm 9$	$160 \pm 132$
2.7262	$617 \pm 219$	$3.0 \pm 0.7$	$56 \pm 17$	$50 \pm 7$	$206 \pm 87$
2.7220	$235 \pm 258$	$2.6 \pm 0.2$	$50 \pm 30$	$40 \pm 19$	$90 \pm 98$
2.7203	$812 \pm 468$	$4.3 \pm 0.6$	$56 \pm 22$	$79 \pm 12$	$189 \pm 112$
2.7183	$2948 \pm 1007$	$21 \pm 0.2$	$43 \pm 10$	$50 \pm 4$	$137 \pm 47$

Table 3. He II Ly $\alpha$  Optical Depths at  $z > 2.77$

Interval	He II Ly $\alpha$ range (Å)	$z$	$\tau(\text{Ly}\alpha)$ <i>FUSE</i>	$\tau(\text{Ly}\alpha)$ STIS	$\tau_{\text{raw}}(\text{Ly}\beta)$ <i>FUSE</i>	$\tau_{\text{cor}}(\text{Ly}\beta)$	$\tau(\text{Ly}\alpha)$ Calculated
(1)	(2)	(3)	(4)	(5)	(6)	(7)	(8)
A	1175.60–1178.00	2.8738	$2.21 \pm 0.20$	$4.00^{+0.67}_{-0.40}$	$1.10 \pm 0.18$	$0.75 \pm 0.18$	$4.7 \pm 1.1$
B	1174.00–1174.90	2.8661	$0.07 \pm 0.05$	$0.07 \pm 0.04$	...	...	...
C	1170.00–1173.50	2.8572	$2.09 \pm 0.15$	$4.80^{+\infty}_{-0.80}$	$1.54 \pm 0.24$	$0.89 \pm 0.28$	$5.5 \pm 1.7$
D	1165.00–1169.90	2.8431	$2.18 \pm 0.14$	$> 4.54$	$1.04 \pm 0.11$	$0.70 \pm 0.13$	$4.3 \pm 0.8$
E	1162.00–1165.00	2.8300	$2.33 \pm 0.18$	$2.86^{+0.39}_{-0.28}$	$0.72 \pm 0.11$	$0.37 \pm 0.14$	$2.3 \pm 0.9$
F	1159.00–1161.00	2.8185	$0.33 \pm 0.03$	$0.44 \pm 0.06$	...	...	...
G	1157.75–1158.25	2.8119	$0.13 \pm 0.06$	$0.24^{+0.12}_{-0.11}$	...	...	...
H	1155.00–1157.75	2.8066	$1.97 \pm 0.12$	$2.34^{+0.40}_{-0.28}$	$0.91 \pm 0.10$	$0.56 \pm 0.13$	$3.5 \pm 0.8$
I	1150.00–1154.95	2.7938	$1.79 \pm 0.07$	$3.72^{+\infty}_{-0.81}$	$1.03 \pm 0.10$	$0.68 \pm 0.13$	$4.3 \pm 0.8$
J	1145.00–1149.95	2.7774	$2.32 \pm 0.12$	$2.57^{+0.72}_{-0.41}$	$0.94 \pm 0.07$	$0.60 \pm 0.10$	$3.8 \pm 0.6$